Scale-dependent characteristics of shear layers in turbulence subject to axisymmetric expansion

Zexu Han (澤旭 韓), Tomoaki Watanabe (渡邉 智昭),[a] and Koji Nagata (長田 孝二)
Department of Mechanical Engineering and Science, Kyoto University, Kyoto 615-8530, Japan

(Dated: 2 July 2026)

The present study experimentally investigates the scale-dependent characteristics of shear layers in turbulence subject to axisymmetric expansion. Turbulence is generated by opposed multiple-jet arrays, in which two opposing nearly homogeneous isotropic turbulent flows collide and form an axisymmetric straining field. Two-dimensional, two-component particle image velocimetry is used to measure velocity fields, and shear layers are analyzed with the triple decomposition applied to filtered velocity gradients with filter sizes on the order of 10^2 times the Kolmogorov scale. Conditional averaging in a local coordinate aligned with shear layers reveals that intense shear is concentrated in layer-like regions. The normalized profile of conditionally averaged shear vorticity is nearly independent of filter size, indicating self-similar shear layers at different scales. The mean velocity jump across the shear layer increases with shear-layer thickness and follows the scaling predicted by Kolmogorov's second similarity hypothesis. The orientation dependence of shear layers is also examined. Shear layers are less frequently observed with orientations nearly parallel to the expansion direction than to the compression axis, and this tendency becomes more pronounced at larger scales. The normalized velocity jump increases as the layer orientation approaches that parallel to the compression axis, indicating that the velocity fluctuations enhanced by axisymmetric expansion in that direction strengthen the shear. The aspect ratio becomes larger for layers nearly perpendicular to the compression axis, suggesting that the imposed strain flattens shear layers depending on their alignment. These results indicate that the anisotropy of shear-layer characteristics induced by axisymmetric expansion becomes more evident at larger scales.

[a] Author to whom correspondence should be addressed: watanabe.tomoaki.8x@kyoto-u.ac.jp

I. INTRODUCTION

Turbulence subject to fluid deformation caused by mean velocity gradients is an important topic in fluid mechanics.[1,2] Depending on the form of the mean velocity gradient tensor $A_{ij} = \partial\langle u_i\rangle/\partial x_j$, defined in terms of the mean velocity $\langle u_i\rangle$, turbulence properties are modified by the deformation. Theoretical studies often consider initially homogeneous isotropic turbulence subject to specific forms of $\partial\langle u_i\rangle/\partial x_j$, such as mean shear, plane strain, and axisymmetric expansion or contraction.[1,3,4] Turbulent flows encountered in engineering applications and environmental settings often evolve under the influence of mean velocity gradients. Large-scale velocity distributions in the ocean and atmosphere generate mean shear, which contributes to turbulence production.[5,6] Flow near the stagnation point around bodies is strongly influenced by mean strain, making this phenomenon relevant to airfoil performance.[7–9] Understanding the effects of mean deformation on turbulence is crucial for the further development of turbulence models and theories.

One of the simplest forms of mean deformation is axisymmetric strain, which is described by

$$\boldsymbol{A} = \begin{pmatrix} \partial\langle u\rangle/\partial x & \partial\langle u\rangle/\partial y & \partial\langle u\rangle/\partial z \\ \partial\langle v\rangle/\partial x & \partial\langle v\rangle/\partial y & \partial\langle v\rangle/\partial z \\ \partial\langle w\rangle/\partial x & \partial\langle w\rangle/\partial y & \partial\langle w\rangle/\partial z \end{pmatrix} = \begin{pmatrix} -S & 0 & 0 \\ 0 & S/2 & 0 \\ 0 & 0 & S/2 \end{pmatrix} \tag{1}$$

where u, v, and w are the velocity components in the x, y, and z directions, respectively. Axisymmetric expansion and contraction are represented by Eq. (1) with $S > 0$ and $S < 0$, respectively. When initially homogeneous isotropic turbulence is subjected to axisymmetric expansion or contraction, the flow becomes increasingly anisotropic. For axisymmetric expansion, the velocity variance in the axial compression direction, $\langle u'^2\rangle$, becomes greater than those in the other expansion directions, $\langle v'^2\rangle$ and $\langle w'^2\rangle$, where $f' = f - \langle f\rangle$ denotes the fluctuating component of f.[10–13] In addition, the longitudinal integral scale of u becomes larger than those of the other components. The opposite trends occur in axisymmetric contraction.[14–20] These changes have been consistently reported in experiments and direct numerical simulations (DNS). Turbulence subjected to axisymmetric strain has also been studied using rapid distortion theory (RDT), which assumes that the mean strain acts on a timescale much shorter than the turbulence timescales.[1,4] Even when the strain and turbulence have comparable timescales, some strain effects observed in experiments and DNS are qualitatively consistent with RDT. However, several important deviations have been reported. RDT predicts an upper bound for the changes in the velocity variance ratios, $\langle u'^2\rangle/\langle v'^2\rangle$ and $\langle u'^2\rangle/\langle w'^2\rangle$.[1] Experiments and DNS under slow strain have consistently reported changes in these ratios that exceed the RDT upper bound.[10,11,13] Another important difference appears in the energy spectrum of velocity fluctuations. At high Reynolds number, RDT predicts that the $-5/3$ law in the inertial subrange remains valid even under axisymmetric strain. However, high-Reynolds-number experiments have shown that the slope of the energy spectrum becomes steeper and more gradual than the $-5/3$ law under axisymmetric expansion and contraction, respectively.[13,16] In addition, the scaling exponent of velocity structure functions in turbulence subjected to axisymmetric expansion differs from that in other turbulent flows.[13] These scale dependencies of turbulent velocity fluctuations in axisymmetric expansion and contraction exhibit significant differences from those in other turbulent flows and deserve further investigation.

One important approach to characterizing turbulence is based on its structures, which appear as characteristic patterns in the distributions of flow variables. Flow structures are commonly identified using quantities defined from the velocity gradient tensor $\partial u_i/\partial x_j$. Previous studies have identified two structures associated with vorticity, depending on the geometry and origin of the vorticity. One is a vortex tube, in which intense vorticity is concentrated in a tubular region.[21] The vorticity in a vortex tube is attributed to rigid-body rotation.[22] Another is a vortex sheet, which has a layer-like shape.[23] A vortex sheet is characterized by shear, which contributes to the vorticity within it.[22,24] Therefore, recent studies often refer to a vortex sheet simply as a shear layer.[25] Early studies of vortical structures focused mainly on vortex tubes, for which various identification methods have been proposed, such as the Q-criterion[26] and the λ_2-criterion[27,28]. Observations of flow fields in coordinates aligned with vortex tubes have revealed various properties, such as their diameter, azimuthal velocity, and vortex stretching induced by the surrounding strain.[29–32] Compared with vortex tubes, shear layers were less investigated in early studies, possibly because of the difficulty in identifying their location and orientation, both of which are essential for observing the local flow pattern around them.

A recent development in shear layer identification has led to extensive research on shear layers in turbulent flows. These studies adopt the triple decomposition of the velocity gradient tensor, which decomposes local fluid motion into three components: elongation, rigid-body rotation, and pure shear.[33] The shear component of the velocity gradient tensor can be utilized to identify the location and orientation of shear layers. The mean flow field observed in a local coordinate aligned with the shear layer has shown that the width and shear-related velocity jump across the shear layer scale with the Kolmogorov length and velocity scales.[25,34,35] Shear layers experience biaxial strain, in which fluid within the shear layer is compressed in the layer-normal direction and stretched in the vorticity direction. The interaction between vorticity due to shear and the surrounding strain contributes to enstrophy production and strain self-amplification, both of which are essential dynamical properties of turbulence.[25] The triple decomposition also splits the vorticity vector into rigid-body rotation and shear components. The velocity fields induced by these two components can be reconstructed using the Biot-Savart law applied to the decomposed vorticity vectors. Analyses based on this velocity decomposition have confirmed that important turbulence characteristics, such as energy cascade and momentum and scalar transfer, are dominated by the shear-induced velocity.[36] The shear layers can become unstable, leading to vortex formation.[23,37–39] This instability process promotes turbulent entrainment and passive-scalar mixing at small scales.[40,41] These analyses of shear layers are based on the triple decomposition applied to the velocity gradient tensor, which is dominated by small-scale velocity fluctuations. The decomposition can also be applied to the gradient of spatially filtered velocity to investigate the scale-dependent properties of shear layers. The scale dependence of shear layers has been investigated using velocity data obtained by two-dimensional, two-component particle image velocimetry (PIV) in nearly homogeneous isotropic turbulence.[42] It was shown that self-similar shear layers exist over a wide range of scales. The velocity jump across shear layers within the inertial subrange was also shown to be predictable based on Kolmogorov's second similarity hypothesis.

Beyond the triple-decomposition-based analyses described above, related approaches have also been developed to characterize local motions from the velocity-gradient tensor. Approaches based on the Schur decomposition have separated normal and non-normal contributions to local velocity-gradient dynamics, showing the importance of non-normal, shear-related motions in homogeneous isotropic turbulence and spatially developing inhomogeneous turbulent flows.[43,44] The Schur-decomposition framework has also provided a standardized real Schur-form formulation of the triple decomposition and has been used to characterize shearing, elongating, and rotating motions in turbulent flow fields.[45,46] In addition, normality-based analyses of filtered velocity gradients using velocity-gradient partitioning have supported the relevance of shear layers to the energy cascade.[47,48]

The previous findings show that axisymmetric strain can modify not only one-point velocity statistics but also scale-dependent velocity fluctuations. These results provide motivation to examine whether turbulence structures associated with scale-dependent motion are also affected by axisymmetric strain. The preceding studies show that shear layers identified by the triple decomposition play an important role in the dynamical properties of turbulence, including enstrophy production, strain self-amplification, energy cascade, and momentum and scalar transfer. However, their scale-dependent characteristics have been investigated mainly in nearly homogeneous isotropic turbulence. It therefore remains unclear whether the self-similar structure of shear layers and the scaling of the velocity jump across them are preserved when turbulence is subjected to mean strain. It is also unknown how the anisotropy induced by axisymmetric expansion affects the orientation and geometry of shear layers. The present study addresses this issue by experimentally investigating the scale-dependent characteristics of shear layers in turbulence subject to axisymmetric expansion generated by opposed multiple-jet arrays (OMJA). The OMJA facility was developed in our previous study to experimentally realize turbulence subject to axisymmetric expansion. Each of the two opposing jet arrays generates nearly homogeneous isotropic turbulence in a duct. The collision of the two opposing turbulent flows creates an axisymmetric straining field into which the turbulent flows enter. Using this facility, the present study experimentally investigates the scale-dependent characteristics of shear layers under the influence of axisymmetric expansion.

The paper is organized as follows. Section II provides an overview of the experimental setup, including the OMJA facility and measurement details. Section III describes the shear layer analysis based on the triple decomposition of the filtered velocity gradient tensor. Section IV presents the characteristics of shear layers at different scales. Finally, the main findings are summarized in Sec. V.

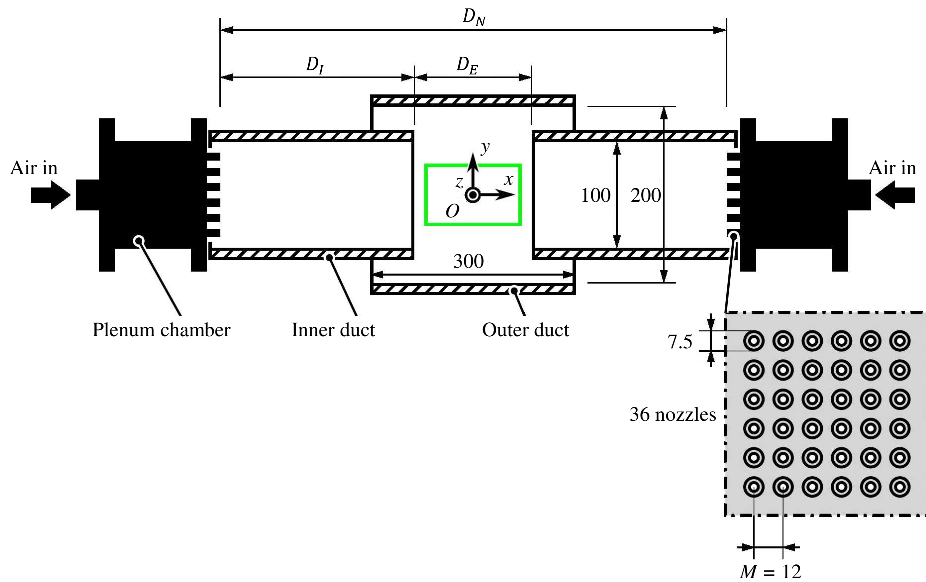

FIG. 1. Schematic illustration of the opposed multiple-jet arrays (OMJA). All dimensions are given in mm.

II. VELOCITY MEASUREMENTS OF TURBULENCE GENERATED BY OPPOSED MULTIPLE-JET ARRAYS

The present study analyzes velocity datasets of turbulence subject to axisymmetric expansion in the OMJA facility, obtained in our previous study,[13] in which measurements were conducted using two-dimensional, two-component PIV.[13] Our previous study presented details of the facility and the PIV system and revealed anisotropy induced by axisymmetric expansion through conventional velocity statistics, such as mean velocity, Reynolds stress, and energy spectra.[13] The experiments reported in Ref. 13 are briefly described here. The present study investigates shear layers across different scales, which could not be assessed from the results presented in our previous study.[13]

A. Opposed multiple-jet arrays

Figure 1 shows a schematic of the OMJA facility.[13] It has a symmetric layout with two multiple-jet generators and a test section consisting of inner and outer ducts. The x, y, and z directions are aligned with the jet direction, the vertical direction, and the remaining orthogonal direction, respectively, and the origin is set at the center of the test section. Each jet generator consists of a plenum chamber and an air supply system. The chamber has an inner diameter of 155.2 mm and a length of 160 mm. Each plenum chamber is equipped with Laval nozzles arranged in a 6×6 array with a center-to-center spacing of $M = 12$ mm. Each nozzle has a throat diameter of 4.12 mm, an outlet diameter of 4.31 mm, and an inlet diameter of 6.3 mm. The nozzle outer diameter is 7.5 mm. Two 400 l air tanks (Anest Iwata, SAT-400C-140) are connected to the plenum chambers via moisture separators (SMC, AF800-14), pressure regulators (SMC, AR825-14G), and solenoid valves (SMC, VXP2380-14-5G). Prior to the experiments, compressed air with a gauge pressure of approximately 0.9 MPa is stored in each tank using oil-free compressors (Anest Iwata, TFP75CF-10) through refrigerant-type dryers (Orion Machinery, RAX8J-SE-A1). The compressed air is supplied to the plenum chambers from the backplate when the valves are opened. The pressure regulators are adjusted to maintain the plenum pressure at 300 kPa in absolute pressure, for which the nozzles are designed to generate fully expanded supersonic jets with a Mach number of 1.36, corresponding to a jet velocity of 404 m/s. Unless otherwise noted, pressure values in this paper are given as absolute pressures. The pressure in the test section is approximately atmospheric; our previous measurement showed that the mean gauge pressure at the test-section center is approximately 10^2 PaG, which is much smaller than atmospheric pressure.[13] The jet Mach number was verified using the Prandtl formula[49] applied to schlieren visualizations near the nozzles in our previous study.[50] The jet Reynolds number, based on the jet velocity and nozzle outlet diameter, is 1.9×10^5.

The inner and outer ducts have square cross sections with internal dimensions of 100×100 mm^2 and 200×200 mm^2, respectively. The inner ducts are connected to the front of the plenum chambers. In each inner duct, the interaction of 36 jets generates decaying nearly homogeneous isotropic turbulence, and its formation process through jet interaction has been investigated in previous studies.[50–53] Two incoming turbulent flows collide between the ends of the two inner ducts and enter the outer duct while spreading radially. Eventually, the flow is ejected from the end of the outer duct. The collision of the opposing flows forms a stagnation region and thus generates axisymmetric strain, with compression in the jet-flow direction and expansion in the radial direction. The properties of the strain field and the incoming turbulent flows depend on the test section geometry. Experiments were conducted for six different sets of the inner duct length D_I and the nozzle-to-nozzle spacing between the two jet arrays, D_N. These two parameters determine the gap between the inner duct ends, defined as $D_E = D_N - 2D_I$. These lengths are illustrated in Fig. 1.

Although the ducts and nozzle arrays have square cross sections, the term axisymmetric expansion in this study refers to the measured mean-strain field, rather than to the exact geometry of the facility. The square nozzle arrangement is used to generate nearly homogeneous isotropic turbulence through multiple-jet interaction in the inner ducts. The axisymmetric strain is produced by the collision of the opposed turbulent flows and their subsequent spreading in the transverse directions from the inner ducts to the outer duct. In our previous study using the same OMJA facility[13], the mean velocity-gradient tensor was shown to satisfy $A_{xx} : A_{yy} : A_{zz} = -2 : 1 : 1$ in the central measurement region, approximately for $|x/M| < 3$ and $|y/M| < 1.5$, where x is the compression axis and the y and z directions correspond to the expansion directions. The transverse extent of this measurement region is well within the inner-duct cross section of $(8.3M)^2$ and is away from the duct walls. Although the facility itself is not geometrically axisymmetric, the flow analyzed in the present study is well approximated by axisymmetric expansion in terms of the mean-strain field.

B. Velocity measurements

Velocity measurements were conducted using PIV near the center of the test section. Tracers were seeded into the incoming turbulent flows by ethanol condensation. A small amount of ethanol was evaporated into the air within the plenum chambers. Fluid expansion in the Laval nozzles leads to ethanol condensation, generating tracer particles. This seeding technique, based on condensation in nozzles, has been widely used in high-speed flows because it generates very fine particles with diameters as small as 10^3 nm.[50,54–56] For turbulence generated with the OMJA facility, the particle Stokes number is small enough for the particles to act as accurate tracers.[13]

As the light source, the present PIV system used a double-pulse Nd:YAG laser (Dantec Dynamics, Dual Power 65-15). Particle images on the x–y plane at $z = 0$ were captured by a high-speed camera (Dantec Dynamics, SpeedSense 9070) equipped with a macro lens (Nikon, AI AF Micro Nikkor 105 mm F2.8D). The camera has a resolution of 1280×800 pixels. The approximate field of view (FOV) of the PIV measurements is indicated by the green squares in Fig. 1. The laser and camera were controlled with a synchronizer (Dantec Dynamics, 80N77) via the PIV software (Dantec Dynamics, DynamicStudio). The velocity measurements were conducted at a sampling frequency of 15 Hz. The particle images were processed using an adaptive PIV algorithm[57] and universal outlier detection[58] in the PIV software to obtain velocity vectors. The minimum and maximum interrogation window sizes were 16×16 and 32×32 pixels, respectively. The resulting vector spacing was 8 pixels, with 50% overlap for the minimum window. More than 1000 velocity fields were obtained by repeating the experiments.

The interval between two laser pulses was adjusted between 3 and 6 μs depending on the case to maintain an average particle displacement of about 2–3 pixels. Each laser pulse had a width of less than 4 ns. The velocity measurements were conducted at a sampling frequency of 15 Hz. The experiments were repeated 12–13 times for each case, yielding more than 1000 velocity fields per case.

The duration of one operation of the OMJA facility is limited by the capacity of the air tanks. The plenum pressure reaches the target value within less than 0.2 s after valve operation and remains within $\pm 5\%$ of the target value for about 6 s, as reported in our previous study.[13] Schlieren visualization also confirmed that the jets are established by 0.25 s.[50] All PIV measurements were conducted within this period. At the sampling frequency of 15 Hz, approximately 90 velocity fields were obtained in each operation of the OMJA facility. The velocity statistics are evaluated using ensemble averages of statistically independent velocity fields, rather than time averages from a single run. The sampling interval of the PIV measurements was 0.067 s, whereas the characteristic time scale of large-scale turbulent motions, estimated from the ratio of the integral length scale to the rms velocity fluctuation, was about 0.002 s. Therefore, velocity fields obtained from consecutive particle-image pairs are considered statistically independent. Because the present PIV measurements are not time-resolved, the present study does not discuss the temporal evolution of turbulence, such as spectral evolution and phase information.[59]

TABLE I. Experimental parameters and turbulence properties.

Case	1	2	3	4	5	6
D_N (mm)	930	930	930	725	725	725
D_E (mm)	80	100	120	80	100	120
D_I (mm)	425.0	415.0	405.0	322.5	312.5	302.5
A_{xx} (1/s)	-7.2×10^2	-6.4×10^2	-6.0×10^2	-8.3×10^2	-7.0×10^2	-7.3×10^2
A_{yy} (1/s)	3.5×10^2	3.2×10^2	3.0×10^2	4.1×10^2	3.5×10^2	3.6×10^2
$A_{yy}/\lvert A_{xx}\rvert$	0.49	0.50	0.50	0.49	0.50	0.49
u_{rms} (m/s)	16.6	18.4	19.5	28.1	27.6	29.5
v_{rms} (m/s)	11.4	12.3	12.4	17.8	17.3	17.9
$u_{\mathrm{rms}}/v_{\mathrm{rms}}$	1.5	1.5	1.6	1.6	1.6	1.7
L_u (mm)	27.6	30.0	34.8	28.8	33.6	34.8
L_v (mm)	22.8	20.4	19.2	19.2	18.0	16.8
L_u/L_v	1.2	1.5	1.8	1.6	1.9	2.0
ST	1.2	1.0	1.0	0.84	0.76	0.76
L_u/η	2.0×10^3	2.5×10^3	2.9×10^3	3.2×10^3	3.6×10^3	3.9×10^3
Re_λ	5.7×10^2	6.0×10^2	6.3×10^2	7.1×10^2	7.2×10^2	7.3×10^2

Velocity statistics are evaluated using ensemble averages, denoted by $\langle f \rangle$, as functions of (x, y). The rms values of fluctuating quantities f' are evaluated as $f_{\mathrm{rms}} = \langle f'^2 \rangle^{1/2}$. In addition, spatial averages are taken when bulk flow properties are examined. Statistical errors are estimated by evaluating velocity statistics using reduced samples. Specifically, the velocity datasets are divided into two sets, and the differences between the statistics obtained from each set are presented as error bars.

C. Experimental conditions and basic flow properties

In the inner ducts, nearly homogeneous isotropic turbulence decays with distance from the jet nozzles. Therefore, D_N is relevant to the properties of the incoming turbulent flows that enter the strain region. From the end of the inner duct, the mean velocity decreases to zero at the stagnation point. Therefore, the mean velocity gradient, which measures the strength of the axisymmetric strain, varies with the gap $D_E = D_N - 2D_I$. Based on these considerations, the experiments were conducted for six cases with different sets of D_I and D_N, as summarized in Tab. I. Table I also presents the basic flow properties based on PIV measurements reported in Ref. 13. Our previous studies have also presented other statistics in the OMJA facility, such as spatial distributions of velocity statistics and energy spectra, as well as the decay characteristics of turbulence in the inner duct.[13,50]

The development of turbulence downstream of the nozzles was examined in our previous study using the same multiple-jet generator.[13,42,50] The vertical profiles of rms velocity fluctuations at $24M$ and $33M$ downstream of the nozzles, slightly upstream of the inner-duct ends in the present OMJA experiments, were shown to be almost uniform. In addition, the ratio between the streamwise and vertical rms velocity fluctuations in the incoming duct flow was about 1.1–1.2, which is close to the values typically reported for turbulence generated by grids and jet interactions.[52,53,60–63] Thus, the turbulence generated by each jet array has already reached a nearly homogeneous and approximately isotropic state before entering the mean-strain region. In the present OMJA facility, the inner-duct length D_I is larger than $25M$ for all cases. Therefore, the turbulent flow generated by each jet array has sufficiently developed before reaching the inner-duct exit.

The mean velocity gradients $A_{xx} = \partial\langle u\rangle/\partial x$ and $A_{yy} = \partial\langle v\rangle/\partial y$ are negative and positive, respectively, representing compression in the x direction and expansion in the y direction. Axisymmetric strain satisfies $A_{yy} = -A_{xx}/2$, which is also observed in the experimental results. The continuity equation further yields $A_{yy} = A_{zz} = -A_{xx}/2$, which was also confirmed by velocity measurements on the x–z planes in our previous study.[13]

Table I shows the rms velocity fluctuations u_{rms} and v_{rms} and the longitudinal integral scales L_u and L_v. The rms values are defined as $f_{\mathrm{rms}} = \langle f'^2\rangle^{1/2}$. The integral scales are evaluated by integrating the corresponding longitudinal autocorrelation functions. For all cases, u_{rms} is greater than v_{rms}, and L_u is greater than L_v. Numerical simulations and rapid distortion theory have consistently shown that axisymmetric expansion leads to $u_{\mathrm{rms}} > v_{\mathrm{rms}}$ and $L_u > L_v$.[1,4] The present study investigates whether such anisotropy arising from axisymmetric expansion affects the scale-dependent characteristics of shear layers.

Although the jet Mach number is 1.36 at the nozzle exits, compressibility mainly affects the initial development of the supersonic jets near the nozzles. Previous measurements using the same multiple-jet generator showed that the jets rapidly mix with the surrounding fluid, and nearly homogeneous isotropic turbulence is formed at about 0.35 m downstream of the nozzles in the inner duct.[50] At this location, the mean-flow Mach number $M = \langle u \rangle / a$ is about 0.12, and the turbulent Mach number $M_T = (u_{rms}^2 + 2v_{rms}^2)^{1/2}/a \simeq \sqrt{3}u_{rms}/a$ is about 0.09, where $\langle u \rangle$ is the mean velocity, u_{rms} is the root mean square value of streamwise velocity fluctuations, and a is the speed of sound corresponding to the mean temperature.[50] Therefore, the flow in the measurement region far from the nozzles is in a low-Mach-number regime, and local compressibility effects are negligible. In addition, inertial-range statistics of turbulence generated by a single multiple-jet array, such as the $k^{-5/3}$ law of the energy spectra and anomalous scaling of high-order turbulence statistics, were shown to be consistent with those of incompressible turbulence.[42] For the OMJA facility, the mean continuity equation for an incompressible flow was also examined by PIV measurements on the x–y and x–z planes.[13] It was confirmed that $\partial\langle u \rangle/\partial x + \partial\langle v \rangle/\partial y + \partial\langle w \rangle/\partial z = 0$ is satisfied under the present experimental conditions. Thus, Eq. (1) provides an appropriate description of the mean strain in the present measurement region, and the conclusions of this study are not affected by compressibility.

The strain rate is quantified by the mean velocity gradient as $S = (-A_{xx}+2A_{yy}+2A_{zz})/3$, with $A_{zz} = A_{yy}$. The timescale of large-scale turbulent motions is estimated as $T = L/U$, where the relevant length and velocity are defined as $L = (L_u + L_v + L_w)/3$ and $U = [(u_{\rm rms}^2 + v_{\rm rms}^2 + w_{\rm rms}^2)/3]^{1/2}$, with $L_w = L_v$ and $w_{\rm rms} = v_{\rm rms}$. The timescale ratio between the strain and turbulence at large scales is denoted by ST, which is also listed in Tab. I. When the strain acts on turbulence on a much shorter timescale, $ST \gg 1$. In the present study, ST varies between 0.76 and 1.2, indicating that the strain timescale is comparable to the turbulence timescale.

The Kolmogorov scale $\eta = \nu^{3/4}\varepsilon^{-1/4}$ is evaluated using the turbulent kinetic energy dissipation rate ε, which is estimated as $\varepsilon = AU^3/L$ with $A = 1$. Here, ν is the kinematic viscosity. This estimate is used only to evaluate the order of the Kolmogorov scale, because A is not strictly equal to 1, although $A = O(10^0)$ is generally accepted.[26] As shown in Tab. I, the ratio between L_u and η is of the order of 10^3. The PIV resolution, defined as the vector spacing δ, is about 40η–70η, which is comparable to the Taylor microscale.[13] The PIV measurements do not resolve the smallest-scale velocity fluctuations. However, the resolution is sufficient to examine velocity statistics at intermediate scales, such as those in the inertial subrange, as confirmed in our previous study.[42]

The turbulent Reynolds number Re_λ is defined using the Taylor microscale $\lambda = \sqrt{15U^2\nu/\varepsilon}$ as $Re_\lambda = U\lambda/\nu$, and its values are listed in Tab. I. The Reynolds number is about 570–730, which is high enough to examine the scale dependence of turbulent motions.

III. SHEAR LAYER ANALYSES WITH THE TRIPLE DECOMPOSITION

A. Evaluation of scale-dependent shearing motion

The velocity gradient tensor describes local fluid motion around a point. Similarly, the filtered velocity gradient tensor, defined by applying a low-pass filter to the velocity field, describes local motion at the filter cutoff scale. The present study analyzes the low-pass filtered velocity field measured by PIV with the triple decomposition. The low-pass filtering and triple decomposition are local kinematic operations applied to the measured velocity-gradient tensor and do not require the assumption of homogeneous isotropic turbulence. In the present study, these procedures are applied to turbulence subject to axisymmetric expansion in order to examine the effects of the mean strain on shear-layer properties.

A Gaussian filter is applied to the fluctuating velocity fields. The filter operation is defined using a Gaussian low-pass filter kernel $G(r, L_F)$ with filtering scale L_F, introduced in Ref. 1, as

$$G(r, L_F) = \sqrt{\frac{6}{\pi L_F^2}} \exp\left(-\frac{6r^2}{L_F^2}\right). \tag{2}$$

The filtered velocity fluctuations $(\tilde{u}', \tilde{v}')$ are then calculated as

$$\tilde{u}'(x, y; L_F) = \int_{-L_F}^{L_F}\int_{-L_F}^{L_F} G(r, L_F) u'(X, Y)\,\mathrm{d}X\,\mathrm{d}Y, \tag{3}$$

$$\tilde{v}'(x, y; L_F) = \int_{-L_F}^{L_F}\int_{-L_F}^{L_F} G(r, L_F) v'(X, Y)\,\mathrm{d}X\,\mathrm{d}Y, \tag{4}$$

$$r = \sqrt{(x-X)^2 + (y-Y)^2}. \tag{5}$$

Here, a cutoff at $X, Y = \pm L_F$ is applied, corresponding to a 3σ truncation of the standard Gaussian kernel. Data points near the boundaries, for which the prescribed integration domain is not fully contained within the FOV, are discarded and excluded from the subsequent analysis.

The triple decomposition considers three types of motion: shear (S), rigid-body rotation (R), and elongation (E). The filtered velocity gradient tensor $\nabla\tilde{\boldsymbol{u}}'$ is decomposed into these components as $\nabla\tilde{\boldsymbol{u}}' = \nabla\tilde{\boldsymbol{u}}'_S + \nabla\tilde{\boldsymbol{u}}'_R + \nabla\tilde{\boldsymbol{u}}'_E$. This differs from the traditional decomposition into symmetric and antisymmetric parts, which are called the rate-of-strain tensor and rate-of-rotation tensor, respectively. The former is influenced by shear and elongation, whereas the latter is influenced by shear and rigid-body rotation. Therefore, these two components alone cannot distinguish the three motions considered in the triple decomposition.

The triple decomposition is applied to $\nabla\tilde{\boldsymbol{u}}'$ using the same algorithm implemented in previous studies.[24,33,42] The triple decomposition begins by identifying the basic reference frame (BRF) at each position. In the BRF, the shear component is extracted as

$$\left(\nabla\tilde{\boldsymbol{u}}_S'^{(B)}\right)_{ij} = \left(\nabla\tilde{\boldsymbol{u}}'^{(B)}\right)_{ij} - \mathrm{sgn}\left[\left(\nabla\tilde{\boldsymbol{u}}'^{(B)}\right)_{ij}\right]\min\left[\left|\left(\nabla\tilde{\boldsymbol{u}}'^{(B)}\right)_{ij}\right|, \left|\left(\nabla\tilde{\boldsymbol{u}}'^{(B)}\right)_{ji}\right|\right], \tag{6}$$

where the superscript (B) denotes quantities evaluated in the BRF. The BRF is not unique in the sense that the decomposition results remain unchanged even in a reference frame obtained by applying a 90° rotational transformation and/or a symmetric transformation to a given BRF. The present study adopts the BRF in which the shear-related velocity gradient $\nabla\tilde{\boldsymbol{u}}_S'^{(B)}$ is expressed as

$$\nabla\tilde{\boldsymbol{u}}_S'^{(B)} = \begin{pmatrix} 0 & |\tilde{\omega}_S| \\ 0 & 0 \end{pmatrix}, \tag{7}$$

where $\tilde{\omega}_S = (\nabla\tilde{\boldsymbol{u}}'_S)_{21} - (\nabla\tilde{\boldsymbol{u}}'_S)_{12}$ denotes the shear vorticity. This frame, where the shear component is expressed in the form of Eq. (7), is convenient for the following shear-layer analysis because it has a common alignment for all shear layers.[42]

One of the BRFs is obtained with the eigenvectors of the rate-of-strain tensor of the filtered velocity field, which is defined as $\tilde{s}_{ij} = (\partial\tilde{u}'_i/\partial x_j + \partial\tilde{u}'_j/\partial x_i)/2$.[24,33,42] The eigenvalues of $\tilde{s}_{ij}$ are denoted by s_1 and s_2, where $s_1 \geq s_2$, and the corresponding eigenvectors are $\boldsymbol{e}_1 = (e_{1x}, e_{1y})$ and $\boldsymbol{e}_2 = (e_{2x}, e_{2y})$. The transformation matrix from the laboratory coordinates $\boldsymbol{x} = (x, y)$ to the principal-axis coordinate system is defined as

$$\boldsymbol{Q}_e = \begin{pmatrix} e_{1x} & e_{1y} \\ e_{2x} & e_{2y} \end{pmatrix}. \tag{8}$$

The BRF is obtained by rotating this principal-axis coordinate system by 45°. With

$$\boldsymbol{Q}_r(\theta) = \begin{pmatrix} \cos\theta & \sin\theta \\ -\sin\theta & \cos\theta \end{pmatrix}, \tag{9}$$

the transformation matrix from the laboratory coordinates to one of the BRFs is $\boldsymbol{Q}_{B0} = \boldsymbol{Q}_r(45°)\boldsymbol{Q}_e$. The velocity gradient tensor in this BRF is obtained as $\nabla\tilde{\boldsymbol{u}}'^{(B0)} = \boldsymbol{Q}_{B0}\nabla\tilde{\boldsymbol{u}}'\boldsymbol{Q}_{B0}^T$, where T denotes the matrix transpose and the superscript $(B0)$ denotes quantities evaluated in this BRF. Additionally, we can obtain the transformation matrix to the BRF where $\nabla\tilde{\boldsymbol{u}}_S'^{(B)}$ is expressed in the form of Eq. (7), denoted by $\boldsymbol{Q}_B$, by applying a 90° rotational transformation and/or a symmetric transformation to $\boldsymbol{Q}_{B0}$ as needed. Specifically, $\boldsymbol{Q}_B$ is obtained as $\boldsymbol{Q}_B = \boldsymbol{Q}_2\boldsymbol{Q}_1\boldsymbol{Q}_{B0}$, where $\boldsymbol{Q}_1$ and $\boldsymbol{Q}_2$ are given by

$$\boldsymbol{Q}_1 = \begin{cases} \boldsymbol{Q}_r(90°) & \text{when } \; |(\nabla\tilde{\boldsymbol{u}}_S'^{(B0)})_{12}| = 0, \\ \boldsymbol{I} & \text{otherwise,} \end{cases} \tag{10}$$

and

$$\boldsymbol{Q}_2 = \begin{cases} \boldsymbol{Q}_{sym} & \text{when } \; (\boldsymbol{Q}_1\nabla\tilde{\boldsymbol{u}}_S'^{(B0)})_{12} < 0, \\ \boldsymbol{I} & \text{otherwise,} \end{cases} \tag{11}$$

where $\boldsymbol{I}$ is the identity tensor and $\boldsymbol{Q}_{sym}$ is a symmetric transformation matrix written as

$$\boldsymbol{Q}_{sym} = \begin{pmatrix} 1 & 0 \\ 0 & -1 \end{pmatrix}. \tag{12}$$

This derivation of $\boldsymbol{Q}_B$ is based on the characteristics of $\nabla\tilde{\boldsymbol{u}}_S'$, which has only one non-zero component in the basic reference frame, either $(\nabla\tilde{\boldsymbol{u}}_S'^{(B0)})_{12}$ or $(\nabla\tilde{\boldsymbol{u}}_S'^{(B0)})_{21}$[33].

The filtered velocity gradient tensor in the BRF is expressed as $\nabla\tilde{\boldsymbol{u}}'^{(B)} = \boldsymbol{Q}_B\nabla\tilde{\boldsymbol{u}}'\boldsymbol{Q}_B^T$. After the shear component is extracted with Eq. (6), the components of rigid-body rotation and elongation are obtained as the antisymmetric and symmetric parts of the residual tensor after shear extraction, $\nabla\tilde{\boldsymbol{u}}'^{(B)} - \nabla\tilde{\boldsymbol{u}}_S'^{(B)}$, respectively. These decomposed terms in the BRF are then transformed back to the original laboratory coordinate system using the inverse of $\boldsymbol{Q}_B$.

B. Conditional statistics of shear layers

The flow field around intense shear is investigated using the filtered velocity field. The shear intensity is evaluated as the norm of $\nabla\tilde{\boldsymbol{u}}_S'$, $\tilde{I}_S = \sqrt{2(\nabla\tilde{\boldsymbol{u}}_S')_{ij}(\nabla\tilde{\boldsymbol{u}}_S')_{ij}}$. The present study examines the mean flow pattern around local maxima of $\tilde{I}_S$, which appear within shear layers. Here, local maxima with small $\tilde{I}_S$ are excluded to mitigate the effects of measurement errors.

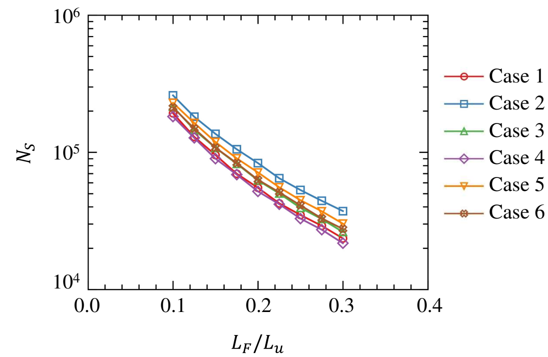

FIG. 2. The number of detected shear layers, N_S, for different filter sizes L_F.

Specifically, only local maxima satisfying $\tilde{I}_S > C_{th}\langle\tilde{I}_S\rangle$ are taken into account in evaluating the statistics of shear layers. A previous study also investigated shear layers using the same method applied to PIV data of nearly homogeneous isotropic turbulence, where C_{th} was shown not to influence the scale dependence of shear layer properties.[42] Most results are presented for the threshold $C_{th} = 1.5$, while the dependence on C_{th} is also examined in Appendix A, which confirms that the discussion below is not influenced by the specific choice of threshold.

The number of detected shear layers, N_S, depends on the filter size because local maxima of shear intensity are identified from the filtered velocity fields. Figure 2 shows N_S as a function of L_F/L_u for all cases. Although N_S decreases as the filter size increases, it remains larger than 10^4 for all cases and all filter sizes examined in this study. A previous study of conditionally averaged shear-layer statistics reported that the mean shear-layer properties are insensitive to the number of samples over the range 10^3–10^7.[34] The present sample number is therefore sufficient for evaluating the conditionally averaged shear-layer statistics.

The local flow pattern of different shear layers is observed in the basic reference frame defined with $\boldsymbol{Q}_B$, where the shear is represented by Eq. (7). This reference frame, also called the shear coordinate, is denoted by (ζ_1, ζ_2), whose origin is located at the local maxima of $\tilde{I}_S$.

The ζ_1–ζ_2 coordinate system is discretized following the nonuniform mapping function that determines the grid points along the ζ_i direction as

$$\zeta_i(n) = -\frac{\zeta_{\max}}{\alpha_\zeta} \arctan\left[\tanh(\alpha_\zeta)\left(1 - \frac{n + N_\zeta}{N_\zeta}\right)\right], \tag{13}$$

where $n = -N_\zeta, \ldots, N_\zeta$ is the grid index and $N_\zeta = 100$ determines the resolution. The parameter $\alpha_\zeta = 2.5$ controls the stretching of grid points, while $\zeta_{\max} = 7.5L_F$ defines the examined domain size. This procedure results in finer grids near the center, $(\zeta_1, \zeta_2) = (0, 0)$. Flow variables, such as velocity and shear intensity, are interpolated onto the discretized shear coordinate using a third-order Lagrange polynomial interpolation scheme. The velocity vector in the shear coordinate is evaluated by applying the coordinate transformation from the laboratory frame to the BRF to $(\tilde{u}', \tilde{v}')$. Here, the velocity components in the ζ_1 and ζ_2 directions are denoted by $\tilde{u}'_1$ and $\tilde{u}'_2$, respectively. The interpolation onto the shear coordinate is repeated for all local maximum locations. Conditional ensemble averages over all shear layers, denoted by $\overline{f}$, are then taken as functions of (ζ_1, ζ_2).

The shear layers are analyzed on two-dimensional planes, although shear layers in turbulence are intrinsically three-dimensional structures. The present 2D-2C PIV measurements do not provide the complete three-dimensional velocity-gradient tensor. Therefore, the shear layers examined in this study should be interpreted as projected shear-layer signatures on the measurement plane.

The influence of this limitation was examined in our previous study using DNS of homogeneous isotropic turbulence.[42] In the two-dimensional analysis, the absolute value of shear intensity was underestimated because the out-of-plane velocity-gradient components were not included. The mean velocity jump across shear layers was also underestimated because the out-of-plane velocity contribution to the shear-flow velocity was not included. However, the conditionally averaged profiles of shear vorticity and velocity around shear layers are similar between the three- and two-dimensional analyses, and the scale dependence of the velocity jump is well reproduced by the two-dimensional analysis.

To further examine this projection effect in anisotropic turbulence, Appendix B compares three-dimensional and two-dimensional shear-layer analyses using DNS data of a turbulent planar jet. Although the planar jet is different from the present turbulence subject to axisymmetric expansion, it is an anisotropic turbulent flow and is useful for assessing how two-dimensional analyses capture projected shear-layer statistics. The comparison shows that the two-dimensional analysis underestimates the absolute values of shear intensity and velocity

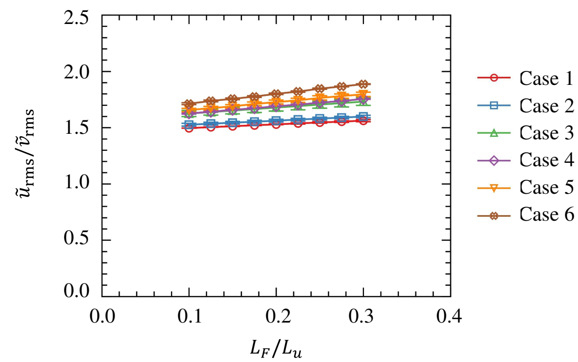

FIG. 3. Ratios of rms velocity fluctuations, $\tilde{u}_{\mathrm{rms}}/\tilde{v}_{\mathrm{rms}}$, at different filter sizes L_F. Here, $\tilde{u}_{\mathrm{rms}}$ and $\tilde{v}_{\mathrm{rms}}$ are evaluated using both ensemble and spatial averages. The error bars indicate statistical uncertainty.

jump because out-of-plane velocity-gradient components and out-of-plane velocity contributions are not included, respectively. However, the normalized shear-intensity profile and the orientation dependence of the velocity jump are similar between the three-dimensional and two-dimensional analyses. These results support the use of the present two-dimensional PIV data to examine the qualitative orientation dependence of projected shear-layer statistics, while confirming that absolute values should be interpreted with caution.

IV. RESULTS AND DISCUSSION

A. Filtered velocity statistics

The basic statistics of filtered velocity fluctuations are presented before discussing the shear layer statistics. Figure 3 shows the ratios of rms velocity fluctuations, $\tilde{u}_{\mathrm{rms}}/\tilde{v}_{\mathrm{rms}}$, as functions of the filter size L_F. For all cases, the ratios are greater than unity over the examined range of L_F, indicating anisotropy induced by the mean strain. As L_F increases, the ratios gradually increase, suggesting stronger anisotropy at larger scales. This behavior is consistent with the classical picture that small-scale motions are less directly influenced by large-scale mean deformation and tend to retain a degree of local isotropization through the energy cascade process.[64]

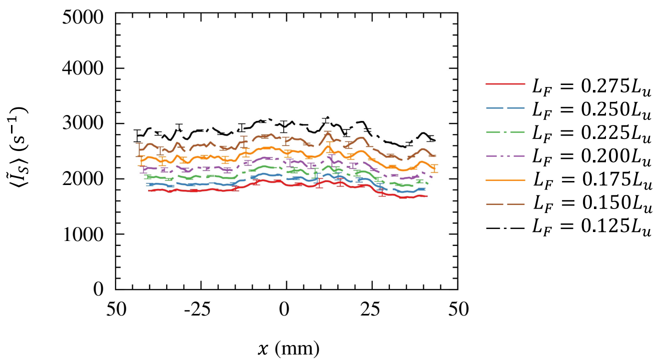

FIG. 4. x distribution of mean shear intensity $\langle \tilde{I}_S \rangle$ at $y = 0$ for various filter sizes in case 2. The error bars are presented at selected locations to visualize statistical uncertainty.

Figure 4 presents the x distribution of mean shear intensity $\langle \tilde{I}_S \rangle$ at $y = 0$ for various filter sizes in case 2. In the OMJA configuration, a turbulent fluid is subjected to the mean strain for a longer time as it is advected from the ends of the inner ducts located at $x = \pm D_E/2$ toward the test section center, $x = 0$. This leads to nonuniform distributions of Reynolds stress along the x axis, which become increasingly anisotropic toward the test section center.[13] However, the mean shear intensity evaluated from the filtered velocity exhibits a uniform distribution and is not directly influenced by this large-scale anisotropy of Reynolds stress.

B. Mean flow properties of shear layers

Figure 5 visualizes the shear intensity $\tilde{I}_S$ for the filter size $L_F = 0.15L_u$. Previous studies have reported that intense shear is concentrated in layer-like regions.[25,35,42] The two-dimensional profile in Fig. 5 also exhibits the same tendency in regions of large $\tilde{I}_S$. The local maxima are identified from the two-dimensional profiles of $\tilde{I}_S$. The mean flow properties around these maxima are then investigated using conditional averages in the shear coordinate (ζ_1, ζ_2).

Figure 6 shows the distribution of the averaged shear intensity $\overline{\tilde{I}_S}$ around shear layers for cases 1 and 4 with the filter size $L_F = 0.2L_u$. The conditionally averaged shear intensity is

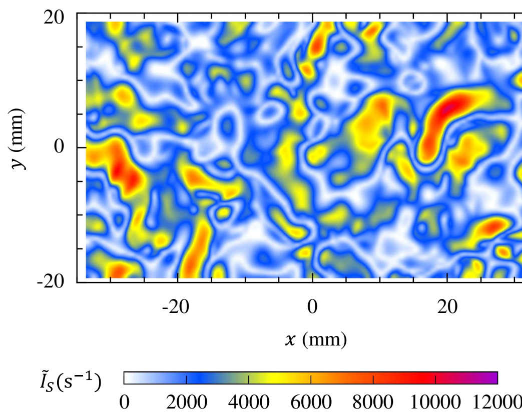

FIG. 5. Shear intensity profile of the filtered velocity at the filter size $L_F = 0.15L_u$ in case 1.

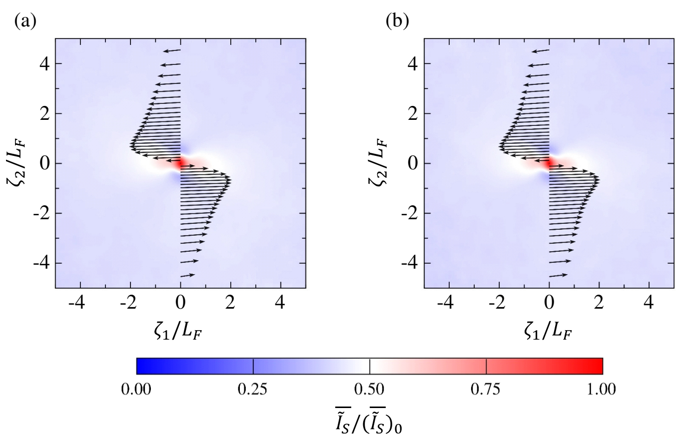

FIG. 6. Conditionally averaged shear layers for the filter size $L_F = 0.2L_u$ in (a) case 1 and (b) case 4. The color contours represent the mean shear intensity $\overline{\tilde{I}_S}$ normalized by its center value $(\overline{\tilde{I}_S})_0$. The black arrows indicate the direction and relative magnitude (arrow length) of the mean velocity vectors on the ζ_2 axis at $\zeta_1 = 0$.

normalized by the corresponding value at $(\zeta_1, \zeta_2) = (0, 0)$, denoted by $(\overline{\tilde{I}_S})_0$. The conditionally averaged velocity vectors $(\tilde{u}_1, \tilde{u}_2)$ calculated on the ζ_2 axis are illustrated with arrows,

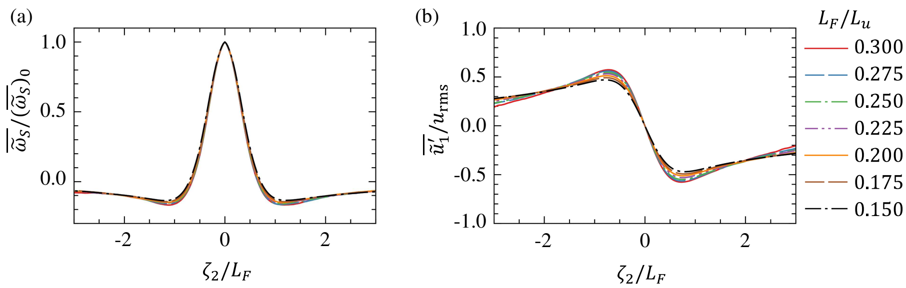

FIG. 7. (a) Normalized conditionally averaged shear vorticity $\overline{\widetilde{\omega}}_S$ and (b) conditionally averaged velocity in the ζ_1 direction, $\overline{\widetilde{u}_1'}$, across the shear layers in case 1. In (a), $\overline{\widetilde{\omega}}_S$ is normalized by the corresponding center value at $(\zeta_1, \zeta_2) = (0, 0)$, denoted by $(\overline{\widetilde{\omega}}_S)_0$.

whose lengths represent the vector magnitude. Large shear intensity is observed in a layer parallel to the ζ_1 direction. Both cases with different test section geometries yield almost identical distributions.

Figure 7(a) examines shear layers at different scales using the profile of the conditionally averaged shear vorticity $\overline{\widetilde{\omega}_S}$ along the ζ_2 axis. The conditionally averaged shear vorticity is normalized by the center value $(\overline{\widetilde{\omega}_S})_0$, while ζ_2 is normalized by the filter size. The conditionally averaged shear vorticity is large within the shear layer located at $|\zeta_2/L_F| \lesssim 1$. This spatial extent of the shear layer does not change with L_F, indicating that shear layers of size L_F are effectively identified from filtered velocity gradients. The normalized distributions of the conditionally averaged shear vorticity are almost identical for different filter sizes, indicating that the shear layers are self-similar over the examined range of scales.

Figure 7(b) presents the conditionally averaged velocity in the ζ_1 direction, $\overline{\widetilde{u}_1}$, normalized by the rms velocity fluctuation u_{rms}, across the shear layers at different scales. The conditionally averaged velocity changes rapidly across the shear layer, exhibiting peaks on both sides. The difference in the conditionally averaged velocity across the shear layer changes with the filter size, indicating that the velocity jump across the shear layers varies with scale.

Three parametric descriptions of the conditionally averaged flow field around shear layers are introduced: the thickness δ_S, the velocity jump Δu, and the aspect ratio A_R. The shear-layer thickness δ_S is defined as the half-width of $\overline{\widetilde{\omega}_S}(\zeta_2)$ at $\zeta_1 = 0$, shown in Fig. 7(a). The velocity jump Δu is then defined as $\Delta u = \delta_S(\overline{\widetilde{\omega}_S})_0$, where the shear vorticity at the

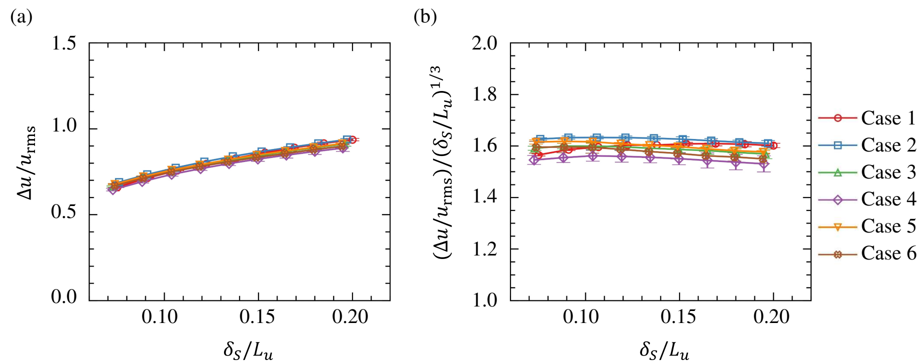

FIG. 8. Relation between the mean velocity jump Δu and the thickness δ_S of shear layers obtained with different filter sizes L_F. The mean velocity jump is normalized by (a) the rms velocity fluctuation u_{rms} and (b) $u_{\mathrm{rms}}(\delta_S/L_u)^{1/3}$. The error bars indicate statistical uncertainty.

shear-layer center, $(\overline{\tilde{\omega}_S})_0$, is equal to the conditionally averaged velocity gradient associated with shear. The aspect ratio is defined using the conditionally averaged shear intensity profile $\overline{\tilde{I}_S}(\zeta_1,\zeta_2)$ in Fig. 6. The normalized shear intensity is defined as $\hat{\tilde{I}}_S(\zeta_1,\zeta_2) = (\overline{\tilde{I}_S} - \langle\tilde{I}_S\rangle)/[(\overline{\tilde{I}_S})_0 - \langle\tilde{I}_S\rangle]$, which takes a value of unity at the shear-layer center and decreases to zero toward the far field. The dimension of the shear layer along the ζ_1 axis, L_{S1}, is quantified as the distance between two points where $\hat{\tilde{I}}_S(\zeta_1,0) = 0.1$. Similarly, the dimension along the ζ_2 axis, L_{S2}, is quantified as the distance between two points where $\hat{\tilde{I}}_S(0,\zeta_2) = 0.1$. The aspect ratio is then evaluated as $A_R = L_{S1}/L_{S2}$. Since the conditionally averaged shear-vorticity profiles plotted against ζ_2/L_F are nearly independent of L_F in Fig. 7(a), the half-width in the normalized coordinate is nearly constant. Thus, $\delta_S/L_F = C$, where C is independent of L_F, indicating that δ_S is proportional to the filter size L_F. Therefore, the dependence of δ_S on L_F is not presented below; instead, Δu and A_R are presented as functions of δ_S.

Figure 8(a) presents the relation between Δu and δ_S, which are normalized by u_{rms} and L_u, respectively. The mean velocity jump increases as the layer thickness increases. This tendency is consistent with the general scale dependence of turbulence, where more turbulent kinetic energy is contained at larger scales. In nearly homogeneous isotropic turbulence, it was shown that the scale dependence of the mean velocity jump in the inertial subrange is well predicted by Kolmogorov's second similarity hypothesis.[42] This leads to the scaling

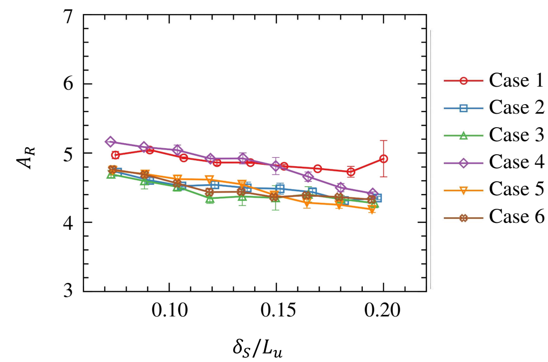

FIG. 9. Relation between aspect ratio A_R and thickness δ_S. The error bars indicate statistical uncertainty.

of $\Delta u \sim (\varepsilon \delta_S)^{1/3}$, which, under the dissipation scaling $\varepsilon \sim u_{\mathrm{rms}}^3/L_u$, can be rewritten as $\Delta u \sim u_{\mathrm{rms}}(\delta_S/L_u)^{1/3}$. Figure 8(b) examines this scaling by plotting $(\Delta u/u_{\mathrm{rms}})/(\delta_S/L_u)^{1/3}$. Here, the examined scale range, $\delta_S/L_u = O(10^{-1})$, corresponds to $\delta_S/\eta = O(10^2)$, which is expected to lie within the inertial subrange. Under this normalization, the mean velocity jump does not vary with δ_S for any of the cases, despite the different degrees of anisotropy arising from axisymmetric expansion. Thus, the mean velocity jump across shear layers follows the prediction based on Kolmogorov's second similarity hypothesis, even under the influence of axisymmetric expansion. This contrasts with the effect of axisymmetric strain on the energy spectrum, for which the inertial-subrange scaling is known to be altered, as discussed in the introduction.

Figure 9 shows the aspect ratio as a function of shear-layer thickness. The aspect ratio depends only weakly on the thickness. The scale independence of the aspect ratio further suggests the self-similarity of shear layers at different scales, which is also indicated in Fig. 7(a).

The range of filter sizes examined in the present OMJA experiment is limited by the spatial resolution of the PIV measurements. To assess whether the observed self-similar shear-layer profile and velocity-jump scaling are robust at different scales, Appendix C compares the present results with additional PIV data obtained in nearly homogeneous isotropic turbulence generated by opposed multiple-fan arrays.[65] The same shear-layer analysis is ap-

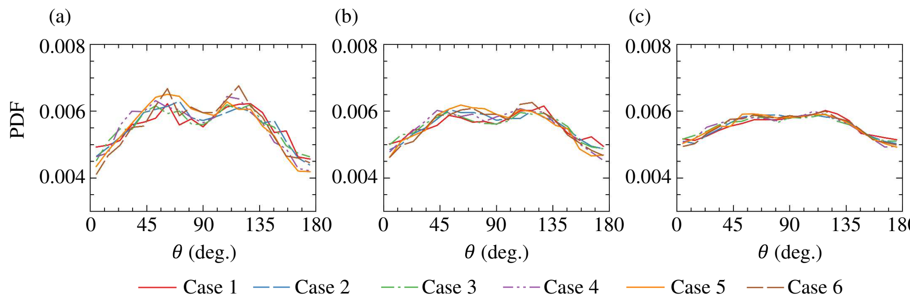

FIG. 10. Probability density functions of θ at different filter sizes: (a) $L_F = 0.3L_u$, (b) $L_F = 0.2L_u$, and (c) $L_F = 0.1L_u$.

plied to both datasets. This comparison extends the examined scale range in Kolmogorov units and shows that the normalized shear-layer profile and the Kolmogorov-scaled velocity jump are consistent between the two experiments.

C. Orientation dependence of shear layers

Axisymmetric expansion leads to larger velocity fluctuations in the x direction than in the other directions. Because this anisotropy may cause shear-layer characteristics to depend on their orientation with respect to the strain direction, we examine the orientation dependence of shear layers. The directional angle θ is defined as the angle between the x direction and the ζ_2 axis of a shear layer. Namely, $\theta = 0°$ and $180°$ when the shear layer is perpendicular to the x direction, whereas the shear layer is parallel to the x direction when $\theta = 90°$.

Figure 10 shows the probability density function (PDF) of θ for three selected filter sizes. The PDF distribution is similar for all cases. The PDF is relatively small near $\theta = 0°$ and $180°$, while it increases over the broad range $45° \lesssim \theta \lesssim 135°$, indicating that shear layers are less frequently aligned parallel to the y direction than to the x direction. Here, the x direction corresponds to the compression axis, while the y direction is one of the transverse expansion directions on the measurement plane. This tendency is consistent with $u_{\rm rms} > v_{\rm rms}$, because shear layers associated predominantly with velocity differences in v are parallel to the y axis. In homogeneous isotropic turbulence, the PDF of θ is expected to be constant. The θ-dependence of the PDF becomes weaker at smaller filter sizes. This indicates

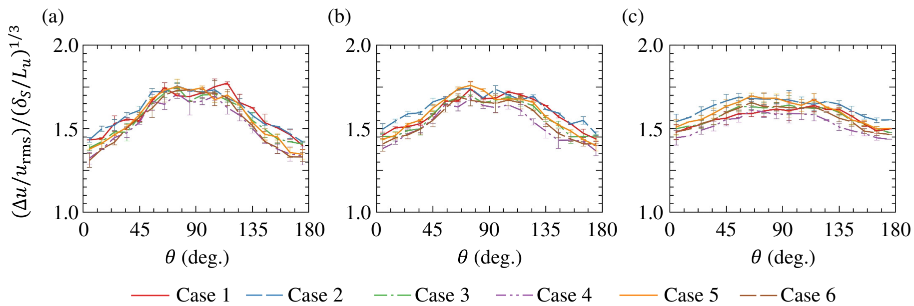

FIG. 11. The θ dependence of the mean velocity jump, Δu, normalized by $u_{\rm rms}(\delta_S/L_u)^{1/3}$ at different filter sizes: (a) $L_F = 0.3L_u$, (b) $L_F = 0.2L_u$, and (c) $L_F = 0.1L_u$. The error bars indicate statistical uncertainty.

that the deviation of shear-layer orientation from an isotropic state is less pronounced at smaller scales. Thus, the influence of axisymmetric expansion on the orientation distribution of shear layers is weaker at smaller filter sizes. Previous experiments on turbulence subject to axisymmetric or planar contraction also reported that vortex tubes preferentially align with a specific direction.[66,67] Thus, both axisymmetric contraction and expansion affect the orientation of vortical structures.

The shear layer statistics are evaluated as functions of θ. Specifically, $0° \leq \theta \leq 180°$ is discretized into 18 bins, and each shear layer is categorized into one of these bins. The conditional averages of shear layers as functions of (ζ_1, ζ_2) are then evaluated using the samples in each θ bin.

Figure 11 examines the θ dependence of the mean velocity jump Δu, normalized by $u_{\rm rms}(\delta_S/L_u)^{1/3}$, for three filter sizes. Here, δ_S is evaluated from averages taken without conditioning on θ. As also observed for the mean velocity jump evaluated over all shear layers, Δu normalized by $u_{\rm rms}(\delta_S/L_u)^{1/3}$ depends only weakly on scale for all cases. However, the normalized velocity jump increases as θ approaches 90°, namely for shear layers parallel to the x direction, which is the compression axis. When a shear layer is parallel to the x direction, the shear arises from the x-directional flow. Axisymmetric expansion intensifies velocity fluctuations in the x direction, leading to a larger velocity jump across shear layers parallel to the x direction. Comparison among the three filter sizes indicates that the θ de-

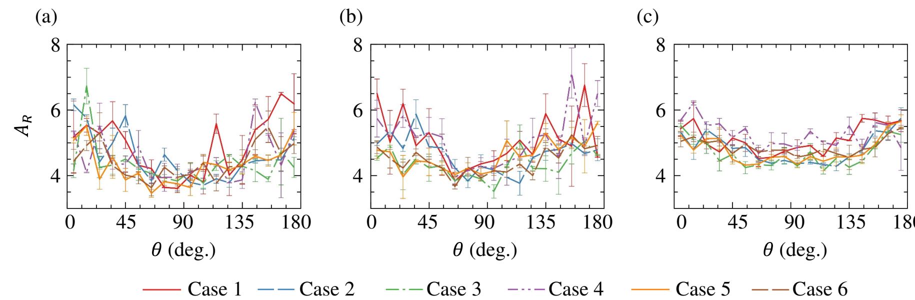

FIG. 12. The θ dependence of the aspect ratio A_R at different filter sizes: (a) $L_F = 0.3L_u$, (b) $L_F = 0.2L_u$, and (c) $L_F = 0.1L_u$. The error bars indicate statistical uncertainty.

pendence is more pronounced at larger scales, suggesting that axisymmetric expansion has a greater impact on larger-scale shear layers. This observation is consistent with the scale-by-scale anisotropy shown in Fig. 3, where velocity fluctuations in the x direction become increasingly larger than those in the y direction as the scale increases.

Figure 12 shows the aspect ratio as a function of angle for three filter sizes. Although oscillations due to statistical uncertainty are not negligible, A_R increases as θ approaches $0°$ and $180°$ from $90°$. Axisymmetric expansion consists of compression in the x direction and expansion in the other directions. Therefore, this behavior of A_R is consistent with the expectation that shear layers become flattened for $\theta \approx 0°$ and $180°$, for which compression and expansion act in the layer-normal and layer-parallel directions, respectively.

V. CONCLUSIONS

The present study experimentally investigated the scale-dependent characteristics of shear layers in turbulence subject to axisymmetric expansion generated by opposed multiple-jet arrays. The analysis was performed using two-dimensional, two-component PIV data and the triple decomposition applied to filtered velocity gradients. The filtered velocity statistics showed that the anisotropy induced by axisymmetric expansion becomes stronger at larger scales, whereas the mean shear intensity remains approximately uniform in space within the measurement region.

Conditional averaging in the shear coordinate showed that intense shear is concentrated in layer-like regions and that the normalized profile of conditionally averaged shear vorticity is nearly independent of filter size. This result indicates that shear layers identified at different filter sizes are self-similar over the examined range. The mean velocity jump across the shear layer increased with shear-layer thickness and followed the scaling predicted by Kolmogorov's second similarity hypothesis. Thus, despite the anisotropy introduced by axisymmetric expansion, the scale dependence of the velocity jump remained consistent with that in nearly homogeneous isotropic turbulence.[42] The aspect ratio depended only weakly on shear-layer thickness, which further supports the self-similar nature of the shear layers.

The orientation dependence of shear layers was also examined. The orientation distribution of shear layers was not uniform: shear layers were less frequently observed with orientations nearly parallel to the expansion direction than to the compression axis, and this tendency became more pronounced at larger filter sizes. The normalized mean velocity jump increased as θ approached 90°, indicating that the deviation of shear-layer characteristics from a homogeneous isotropic state is clearer for shear layers nearly parallel to the compression axis. The aspect ratio increased as θ approached 0° and 180°, suggesting that the imposed strain tends to flatten shear layers depending on their orientation relative to the compressive and extensional strain directions.

These results show that axisymmetric expansion modifies the orientation dependence and anisotropy of projected shear-layer signatures, and that this deviation from a homogeneous isotropic state becomes more pronounced at larger scales. At the same time, the normalized shear-vorticity profile remains nearly independent of filter size and the velocity jump follows the scaling based on Kolmogorov's second similarity hypothesis over the examined range. The present findings provide a new perspective on the structure of turbulence under mean deformation and may contribute to a better understanding of strained turbulent flows.

ACKNOWLEDGMENTS

This work was supported by JSPS KAKENHI Grant No. JP25K01155 and JST SPRING Grant No. JPMJSP2110.

AUTHOR DECLARATIONS

Conflict of interest

The authors have no conflicts to disclose.

Author Contributions

Zexu Han: Data Curation (lead); Formal Analysis (lead); Investigation (lead); Methodology (equal); Software (equal); Validation (equal); Visualization (lead); Writing/Original Draft Preparation (equal); Writing/Review & Editing (equal).

Tomoaki Watanabe: Conceptualization (lead); Data Curation (supporting); Formal Analysis (supporting); Funding Acquisition (equal); Investigation (supporting); Methodology (equal); Project Administration (equal); Resources (equal); Software (equal); Supervision (equal); Validation (supporting); Visualization (supporting); Writing/Original Draft Preparation (equal); Writing/Review & Editing (equal).

Koji Nagata: Conceptualization (supporting); Formal Analysis (supporting); Funding Acquisition (equal); Investigation (supporting); Methodology (equal); Project Administration (equal); Resources (equal); Supervision (equal); Validation (supporting); Writing/Review & Editing (supporting).

DATA AVAILABILITY

The data that support the findings of this study are available from the corresponding author upon reasonable request.

Appendix A: Threshold dependence of shear layer analyses

The shear layer analyses conducted in this study discard local maxima of shear intensity smaller than $C_{th}\langle\tilde{I}_S\rangle$. The dependence of the conditionally averaged shear vorticity and conditionally averaged velocity profiles on C_{th} is presented in Fig. 13. The profiles are insensitive to C_{th} between 1.0 and 3.0, indicating that the threshold does not affect the mean characteristics of shear layers.

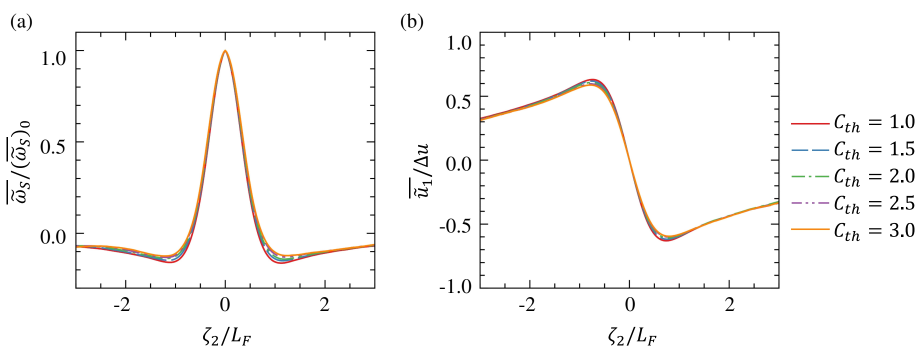

FIG. 13. Threshold dependence of the shear layer analysis. (a) Normalized conditionally averaged shear vorticity $\overline{\tilde{\omega}}_S$ and (b) conditionally averaged velocity in the ζ_1 direction, $\overline{u_1'}$, normalized by the mean velocity jump across the shear layers in case 1 with $L_F = 0.2L_u$.

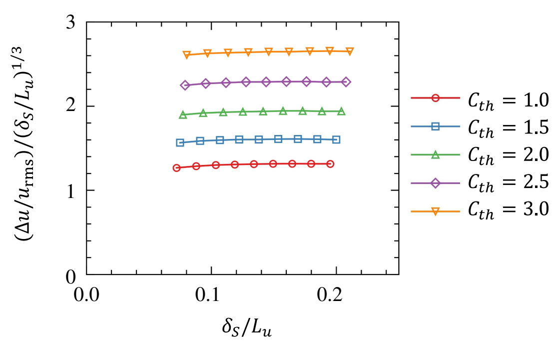

FIG. 14. Threshold dependence of Δu normalized by $u_{\rm rms}(\delta_S/L_u)^{1/3}$ in case 1.

Figure 14 presents Δu normalized by $u_{\rm rms}(\delta_S/L_u)^{1/3}$ for different values of C_{th}. As C_{th} increases, weaker shear layers are excluded from the analysis. Therefore, larger C_{th} leads to larger mean velocity jumps. However, the scale independence of $(\Delta u/u_{\rm rms})/(\delta_S/L_u)^{1/3}$ is observed for different C_{th}, indicating that the discussion in the present study is not sensitive to the choice of C_{th}.

Appendix B: Comparison between three-dimensional and two-dimensional shear-layer analyses

The present study uses two-dimensional, two-component PIV data to investigate projected shear-layer signatures on the measurement plane. As discussed in Sec. III, this analysis does not provide the complete three-dimensional velocity-gradient tensor. Therefore, the absolute values of shear intensity and the velocity jump across shear layers may be underestimated. In addition, orientation-dependent statistics may be affected by projection onto the measurement plane. To examine this issue, we compare three-dimensional and two-dimensional shear-layer analyses using direct numerical simulation (DNS) data of a turbulent planar jet.

The planar jet considered here is not turbulence subject to axisymmetric expansion. However, it is an anisotropic turbulent flow with a mean velocity gradient and is therefore useful for examining projection effects in two-dimensional shear-layer analyses of anisotropic turbulence. The purpose of this appendix is not to reproduce the present OMJA flow, but to assess whether the angle dependence of shear-layer statistics obtained from a two-dimensional projected analysis is consistent with that obtained from the full three-dimensional velocity-gradient tensor. In this appendix, we do not apply the low-pass filter or examine small-scale shear layers, because the Reynolds number in the DNS is much smaller than in the experiments and the scale separation between large and small scales is not sufficient to examine scale dependence.

1. DNS of a temporally evolving turbulent planar jet

We use the DNS database of an incompressible, temporally evolving turbulent planar jet. The DNS details are documented in our previous studies.[34,68] A temporally evolving planar jet is periodic in the streamwise and spanwise directions, and the jet develops in time while spreading in the transverse direction.[69,70] Therefore, the streamwise development of a spatial jet is approximately represented by temporal evolution. Because of the relatively low computational cost of temporal simulations compared with spatial simulations, the temporal configuration has been widely adopted for fundamental studies of turbulent jets.[32,71–76]

The streamwise, transverse, and spanwise directions are denoted by x, y, and z, respectively, and the corresponding velocity components are u, v, and w. The jet Reynolds number is defined as $Re_J = U_J H/\nu$, where U_J is the initial jet velocity, H is the initial jet width, and ν is the kinematic viscosity. The governing equations are the incompressible Navier–Stokes equations. Spatial derivatives are evaluated using fully conservative central-difference schemes, and time integration is performed with a third-order Runge–Kutta method. The fourth- and second-order central-difference schemes are used for the spatial derivatives in the x and z directions and in the y direction, respectively, because nonuniform grid spacing is adopted in the y direction. The pressure Poisson equation is solved using the biconjugate gradient stabilized method. Periodic boundary conditions are imposed in the streamwise and spanwise directions, while free-slip boundary conditions are imposed in the transverse direction.

In this study, we performed a new DNS whose parameters are identical to those in Refs. 34 and 68, except for the streamwise domain size and grid size. The Reynolds number is $Re_J = 4000$. The streamwise domain size is increased to improve statistical convergence of the shear-layer statistics. We also adopted a higher spatial resolution in this study. The computational domain size is $(L_x, L_y, L_z) = (8H, 10H, 4H)$. The number of grid points is $(N_x, N_y, N_z) = (768, 600, 384)$. Other numerical parameters are the same as in our previous studies. The grid spacing is uniform in the x and z directions and nonuniform in the y direction, with finer resolution near the jet centerline. The initial mean streamwise velocity profile is specified with a hyperbolic tangent function following previous studies of turbulent planar jets, while the initial mean velocities in the other directions are zero.[69] Spatially correlated random fluctuations are added to the initial mean velocity field near the jet centerline to trigger transition. The reference time scale of the jet development is defined as $t_r = H/U_J$, which is used to normalize time t.

The planar jet becomes fully turbulent by $t/t_r = 10$.[34] For evaluating conventional velocity statistics, spatial averages are taken over x–z planes and temporal averages are taken over the period $20.29 \leq t/t_r \leq 21.46$, during which instantaneous velocity fields are stored every 20 time steps. The averages are denoted by $\langle f \rangle$ and are obtained as functions of y.

Figure 15 shows the mean streamwise velocity $\langle u \rangle$ normalized by the centerline mean velocity $\langle u \rangle_C$. The transverse position y is normalized by the half-width b_u of $\langle u \rangle$. Because the planar jet is statistically symmetric with respect to $y = 0$, data points on both sides are used to evaluate the mean velocity profile for $y > 0$. The mean velocity profile is compared with previous experiments and DNS of spatially evolving turbulent planar jets. The result of the present temporally evolving simulation agrees well with these previous data.

Figure 16 shows the transverse profiles of rms fluctuations of the streamwise velocity, u_{rms}, and transverse velocity, v_{rms}, normalized by the mean centerline velocity. The normalized rms velocity fluctuations exhibit distributions similar to those reported in previous DNS studies shown in the figure.

The mean velocity profile in Fig. 15 indicates that the mean velocity gradient $\partial\langle u\rangle/\partial y$ becomes large near the jet half-width, $y/b_u = 1$. At this location, turbulence production occurs actively for the streamwise component of turbulent kinetic energy, leading to the peak in the rms streamwise velocity fluctuation u_{rms} shown in Fig. 16.[77–79] Although the pressure-strain correlation redistributes the streamwise component of turbulent kinetic energy to the transverse and spanwise components, u_{rms} remains larger than v_{rms} at $y/b_u = 1$. Because of this anisotropic feature, the shear-layer analyses below are conducted for shear layers located around $y/b_u = 1$. Specifically, shear layers identified in the range $0.9 \leq y/b_u \leq 1.1$ are used as samples for the conditional averages.

At $y/b_u = 1$, $u_{rms}/v_{rms} = 1.4$, which is comparable to the values in turbulence generated by the OMJA facility. At the jet half-width location, both turbulent and non-turbulent fluids appear because of external intermittency.[80] We therefore evaluate the Kolmogorov scales using the kinetic energy dissipation rate averaged over the turbulent fluid. Here, the turbulent fluid is detected as the region where the vorticity magnitude ω exceeds a threshold ω_{th}. Using the mean vorticity magnitude on the jet centerline, $\langle\omega\rangle_C$, the threshold is set to $\omega_{th} = 0.01\langle\omega\rangle_C$. This threshold is determined based on the threshold dependence of the detected turbulent region, as discussed in our previous studies.[34,68] The average evaluated solely over the turbulent fluid is denoted by $\langle f\rangle_T$. The turbulent-fluid average of the kinetic energy dissipation rate is defined as $\langle\varepsilon\rangle_T = \langle 2\nu S_{ij}S_{ij}\rangle_T$, where ν is the kinematic viscosity and S_{ij} is the rate-of-strain tensor. The Kolmogorov length, velocity, and time scales are then evaluated as $\eta = (\nu^3/\langle\varepsilon\rangle_T)^{1/4}$, $u_\eta = (\nu\langle\varepsilon\rangle_T)^{1/4}$, and $\tau_\eta = (\nu/\langle\varepsilon\rangle_T)^{1/2}$. These scales are used to normalize the conditional averages of shear-layer quantities.

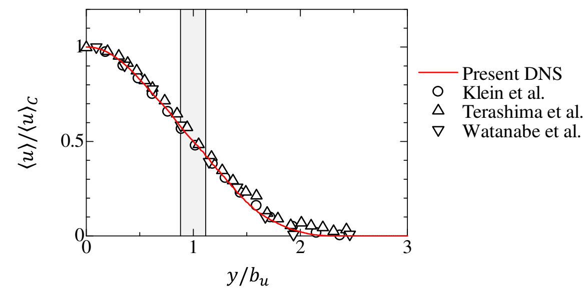

FIG. 15. Mean streamwise velocity $\langle u\rangle$ normalized by the mean centerline velocity $\langle u\rangle_C$. The transverse position y is normalized by the mean velocity half-width b_u. The present results are compared with the DNS of Klein et al.[81] ($Re_J = 4000$) and the experiments of Terashima et al.[82] ($Re_J = 22000$) and Watanabe et al.[83] ($Re_J = 2000$). The gray shaded region indicates the transverse positions where shear layers are analyzed.

2. Three-dimensional shear-layer analysis

The three-dimensional shear-layer analysis is based on the triple decomposition of the full velocity-gradient tensor $\nabla\boldsymbol{u}$, which has been used in our previous studies of temporally evolving planar jets.[34,68] The velocity-gradient tensor is decomposed into shear, rigid-body rotation, and elongation components as $\nabla\boldsymbol{u} = \nabla\boldsymbol{u}_S + \nabla\boldsymbol{u}_R + \nabla\boldsymbol{u}_E$. The decomposition algorithm is the same as that used in our previous studies.[22,85] The shear intensity is defined as $I_S = [2(\nabla\boldsymbol{u}_S)_{ij}(\nabla\boldsymbol{u}_S)_{ij}]^{1/2}$. From the three-dimensional distribution of I_S, shear layers are identified as local maxima of I_S.

For each detected shear layer, a shear coordinate is defined as $(\zeta_1, \zeta_2, \zeta_3)$. The corresponding unit vectors are denoted by $\boldsymbol{e}_1$, $\boldsymbol{e}_2$, and $\boldsymbol{e}_3$. Here, $\boldsymbol{e}_1$ is the direction of the shear vorticity, whose component is defined as $(\boldsymbol{\omega}_S)_i = \epsilon_{ijk}(\nabla\boldsymbol{u}_S)_{jk}$ with the Levi–Civita symbol ϵ_{ijk}. The layer-normal direction and shear-flow direction are denoted by $\boldsymbol{e}_2$ and $\boldsymbol{e}_3$, respectively. Hereafter, the x, y, and z components of $\boldsymbol{e}_\alpha$ ($\alpha = 1, 2, 3$) are denoted by $e_{\alpha x}$, $e_{\alpha y}$, and $e_{\alpha z}$.

With this definition, the shear is represented by the velocity gradient $\partial u_3/\partial\zeta_2$, where u_3 is the velocity component in the ζ_3 direction. The sign ambiguity of the shear coordinate is fixed by imposing $e_{2y} > 0$. The orientation of each shear layer relative to the transverse

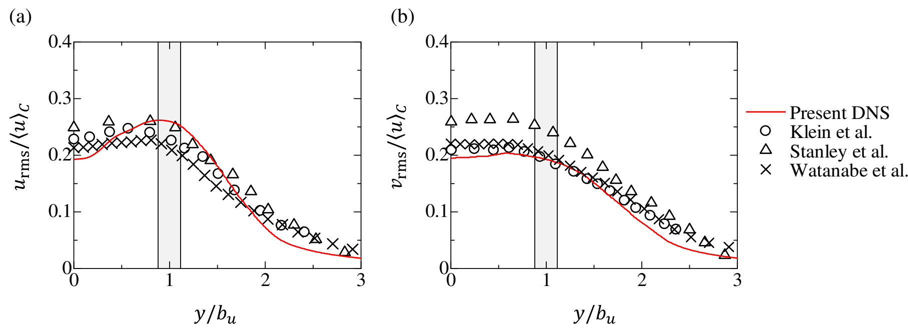

FIG. 16. Transverse profiles of rms velocity fluctuations of (a) streamwise velocity u_{rms} and (b) transverse velocity v_{rms}, normalized by the mean centerline velocity $\langle u\rangle_C$. The transverse position y is normalized by the mean velocity half-width b_u. The present results are compared with the DNS studies of Klein et al.[81] ($Re_J = 4000$), Stanley et al.[77] ($Re_J = 3000$), and Watanabe et al.[84] ($Re_J = 2200$). The gray shaded region indicates the transverse positions where shear layers are analyzed.

direction is quantified by $\cos\phi = \boldsymbol{e}_2 \cdot \boldsymbol{e}_y = e_{2y}$, where $\boldsymbol{e}_y$ is the unit vector in the y direction and ϕ is the angle between the layer-normal direction and the y direction.

Conditional averages around shear layers, denoted by $\overline{f}$, are evaluated as functions of ζ_2 at $(\zeta_1, \zeta_3) = (0, 0)$, representing the profiles of averaged quantities across the shear layer. Here, $0 \leq \cos\phi \leq 1$ is divided into 20 bins, and the conditional averages are evaluated from shear layers in each bin. This procedure allows us to examine the orientation dependence of shear-layer statistics.

3. Two-dimensional shear-layer analysis on x–y planes

To mimic the analysis applied to two-dimensional PIV data, we also perform a two-dimensional shear-layer analysis on x–y planes of the DNS data. In this analysis, only the in-plane velocity components (u, v) and their in-plane gradients are used. The two-dimensional velocity-gradient tensor is decomposed into shear, rigid-body rotation, and elongation components using the same two-dimensional triple-decomposition procedure as that used for the PIV data.

The algorithm for the two-dimensional shear-layer analysis is similar to that for the three-dimensional analysis. The in-plane velocity vector and velocity-gradient tensor are embedded in three-dimensional form as

$$\boldsymbol{u}^{(2D)} = (u, v, 0), \quad \nabla \boldsymbol{u}^{(2D)} = \begin{pmatrix} \partial u/\partial x & \partial u/\partial y & 0 \\ \partial v/\partial x & \partial v/\partial y & 0 \\ 0 & 0 & 0 \end{pmatrix}. \tag{B1}$$

The triple decomposition yields the two-dimensional shear tensor $\nabla \boldsymbol{u}_S^{(2D)}$. The shear intensity I_S is evaluated from this shear tensor, and shear layers are identified as local maxima of I_S on the x–y planes.

The in-plane components of $\nabla \boldsymbol{u}_S^{(2D)}$ are used to determine the shear-coordinate orientations $(\boldsymbol{e}_1, \boldsymbol{e}_2, \boldsymbol{e}_3)$ using the same procedure as that used for the three-dimensional analysis. In the two-dimensional analysis, $\boldsymbol{e}_1$ is parallel to the z direction, while $\boldsymbol{e}_2$ and $\boldsymbol{e}_3$ lie on the x–y plane. A shear coordinate $(\zeta_1, \zeta_2, \zeta_3)$ is then defined for each detected shear layer. The same conditional averaging procedure is applied in this shear coordinate using the in-plane velocity components. The orientation dependence of the projected shear-layer statistics is evaluated from conditional averages as functions of ζ_2 at $(\zeta_1, \zeta_3) = (0, 0)$, which are evaluated separately for different bins of $\cos\phi = e_{2y}$. Here, the notation for the shear coordinate differs from that in Sec. III. In Sec. III, the shear-flow direction is denoted by ζ_1, whereas in this appendix it is denoted by ζ_3 so that the notation is consistent with the three-dimensional shear-coordinate system used in our previous studies.

4. Comparison between three-dimensional and two-dimensional analyses

Figure 17(a) compares the conditionally averaged shear intensity $\overline{I_S}$ obtained from the three-dimensional and two-dimensional analyses for $\cos\phi = 0.88$. In both analyses, $\overline{I_S}$ exhibits a pronounced peak in a thin region around the shear-layer center, indicating that the projected two-dimensional analysis captures the layer-like distribution of shear. However, the magnitude of $\overline{I_S}$ is underestimated in the two-dimensional analysis because the out-of-plane components of the velocity-gradient tensor are not included. The peak values normalized by the inverse of Kolmogorov time scale are 1.31 in the three-dimensional analysis and 0.749 in the two-dimensional analysis. Their ratio is $1.31/0.749 = 1.75$, which is close to $\sqrt{3}$. This

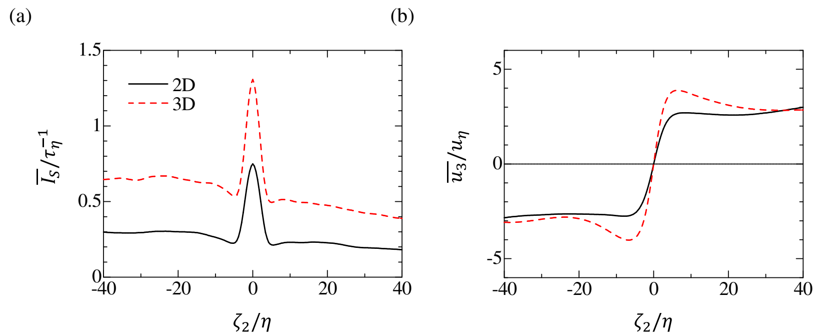

FIG. 17. Conditional averages of (a) shear intensity I_S and (b) velocity in the ζ_3 direction, u_3, for $\cos\phi = 0.88$. The profiles are compared between the three-dimensional and two-dimensional analyses on the x–y plane.

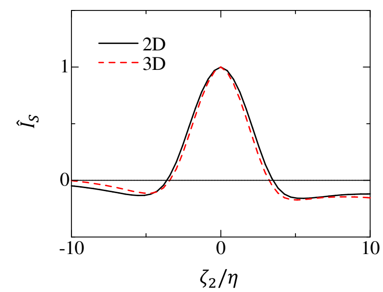

FIG. 18. Normalized conditionally averaged shear intensity $\hat{I}_S = (\overline{I_S} - \langle I_S\rangle)/(\overline{I_{S0}} - \langle I_S\rangle)$ for $\cos\phi = 0.88$. The profiles are compared between the three-dimensional analyses and the two-dimensional analyses on the x–y plane.

ratio is consistent with the factor of $\sqrt{3}$ derived theoretically for isotropic turbulence and confirmed by DNS in Ref. 42.

Figure 17(b) compares the conditionally averaged velocity in the shear-flow direction, $\overline{u_3}$. The conditionally averaged velocity changes rapidly across the shear layer in both the three-dimensional and two-dimensional analyses. However, the velocity jump is smaller in the two-dimensional analysis. This underestimation is attributed to the missing out-of-plane velocity contribution to the shear-flow velocity u_3. Thus, the two-dimensional analysis captures the

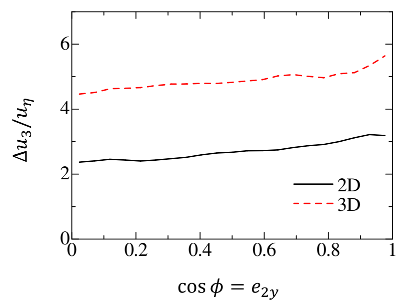

FIG. 19. The mean velocity jump across the shear layer evaluated as a function of the cosine of the angle between the layer-normal direction, $\boldsymbol{e}_2$, and the transverse direction, $\cos\phi = e_{2y}$, where e_{2y} is the y component of $\boldsymbol{e}_2$. The profiles are compared between the three-dimensional analyses and the two-dimensional analyses on the x–y plane.

qualitative mean shear-layer structure but underestimates the absolute values of the shear intensity and velocity jump.

Figure 18 shows the normalized conditionally averaged shear intensity,

$$\hat{I}_S = \frac{\overline{I_S} - \langle I_S \rangle_T}{\overline{I_{S0}} - \langle I_S \rangle_T}, \tag{B2}$$

where $\langle I_S \rangle_T$ is the mean shear intensity in the turbulent region at $y/b_u = 1$, and $\overline{I_{S0}}$ is the conditionally averaged shear intensity at $\zeta_2 = 0$. The normalized shear intensity is equal to 1 at $\zeta_2 = 0$ and decreases toward 0 away from the shear layer. The profiles of $\hat{I}_S$ are nearly identical in the three-dimensional and two-dimensional analyses. Therefore, although the two-dimensional analysis underestimates the magnitude of the shear intensity, it reproduces the normalized distribution of conditionally averaged shear intensity across the shear layer.

The mean velocity jump is evaluated using the half-width of $\hat{I}_S$, denoted by δ_S, and the velocity gradient at the shear-layer center as

$$\Delta u_3 = \delta_S \left. \frac{\partial \overline{u_3}}{\partial \zeta_2} \right|_{\zeta_2=0}. \tag{B3}$$

This definition, originally applied for the velocity jump of each shear layer in Ref. 39, is used in this appendix instead of the definition based on the peaks of the conditionally averaged velocity profile. In the planar jet, the mean streamwise velocity affects the conditionally averaged velocity profile when the layer-normal direction is close to the transverse direction, and the velocity peaks are not always clearly identified. The present definition based on the velocity gradient at the shear-layer center provides a more robust estimate of the velocity jump for examining its orientation dependence.

Figure 19 shows Δu_3 as a function of $\cos\phi = e_{2y}$, where e_{2y} is the y component of the layer-normal unit vector $\boldsymbol{e}_2$. The mean velocity jump decreases as $\cos\phi$ approaches zero, for which the layer-normal direction is nearly perpendicular to the transverse direction. In the turbulent planar jet, the rms velocity fluctuation in the streamwise direction is larger than those in the transverse and spanwise directions.[81,84] When the layer-normal direction is nearly perpendicular to the transverse direction, the shear is less strongly associated with the streamwise velocity component. As $\cos\phi$ increases, the streamwise velocity fluctuations contribute more strongly to the shear, resulting in a larger mean velocity jump.

The two-dimensional analysis gives smaller values of Δu_3 than the three-dimensional analysis, as expected from the comparisons of $\overline{I_S}$ and $\overline{u_3}$ in Fig. 17. Nevertheless, the dependence of Δu_3 on $\cos\phi$ is similar in the three-dimensional and two-dimensional analyses: Δu_3 increases with $\cos\phi$ in both cases. This result indicates that the projected two-dimensional analysis captures the orientation dependence of the shear-layer velocity jump, although its absolute magnitude is underestimated.

This behavior is consistent with the interpretation of the orientation dependence observed in the OMJA experiments. In both the turbulent planar jet and turbulence subject to axisymmetric expansion, the velocity jump tends to be small when the layer-normal direction is perpendicular to the direction of relatively weak velocity fluctuations. In this orientation, the stronger velocity fluctuations contribute less directly to the velocity jump in the shear-flow direction. The present DNS comparison therefore supports the use of projected two-dimensional shear-layer statistics for examining the departure from an isotropic state, while confirming that the absolute values of shear intensity and velocity jump should be interpreted with caution.

Appendix C: Comparison with turbulence generated by opposed multiple-fan arrays

The scale range examined in the present OMJA experiment is restricted by the spatial resolution of the PIV measurements. To examine the robustness of the shear-layer statistics

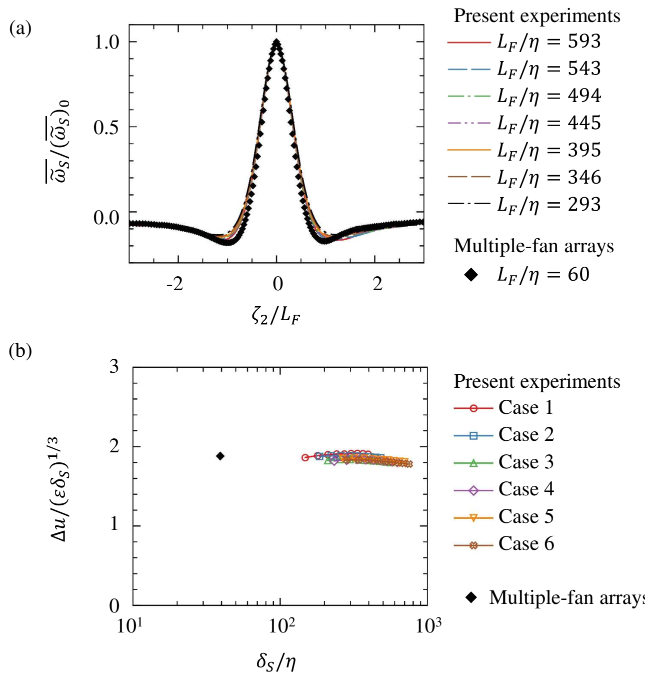

FIG. 20. Comparison between the OMJA experiment and the opposed multiple-fan experiment. (a) Normalized conditionally averaged shear-vorticity profiles across shear layers. (b) Conditionally averaged velocity jump across shear layers normalized by the Kolmogorov scaling, $\Delta u/(\varepsilon \delta_S)^{1/3}$, as a function of δ_S/η.

over a wider range of scales in Kolmogorov units, we compare the present results with velocity data of nearly homogeneous isotropic turbulence generated by opposed multiple-fan arrays.[65] The multiple-fan facility consists of two sets of 9×9 fans installed on opposing faces of a closed rectangular chamber, where nearly homogeneous isotropic turbulence with $Re_\lambda \simeq 120$ is generated. Two-dimensional, two-component PIV was used to measure the velocity field. The same filtering, triple decomposition, and conditional shear-layer analysis as those used for the OMJA data are applied to this dataset.

The filter size normalized by the Kolmogorov scale is $L_F/\eta \approx 198$–1161 ($\delta_S/\eta = 148$–753) in the OMJA experiment, whereas it is $L_F/\eta = 60$ ($\delta_S/\eta = 39$) in the multiple-fan experiment. Thus, the combined datasets allow us to examine whether the mean shear-layer statistics remain consistent at scales smaller than those in the OMJA experiment.

Figure 20(a) compares the conditionally averaged shear-vorticity profiles across the shear layer. The layer-normal coordinate is normalized by the filter size L_F, and the conditionally averaged shear vorticity is normalized by its peak value. The profiles obtained from the OMJA and multiple-fan experiments are nearly identical. This result shows that the conditionally averaged shear-vorticity distribution is nearly independent of the examined scale range, indicating self-similar shear-layer structure over these scales.

Figure 20(b) shows the mean velocity jump across the shear layer normalized by the Kolmogorov scaling, $\Delta u/(\varepsilon\delta_S)^{1/3}$. The normalized velocity jump is approximately 1.9 at $\delta_S/\eta \simeq 39$ in the multiple-fan experiment and approximately 1.8–1.9 for $\delta_S/\eta > 100$ in the OMJA experiments. These values are very close, especially considering that the unnormalized velocity jump expected from $\Delta u \propto \delta_S^{1/3}$ changes by a factor of about 2.7 between $\delta_S/\eta = 39$ and 753. These results support the conclusion that the velocity jump across shear layers is consistent with the Kolmogorov scaling over the examined range.

REFERENCES

[1]S. B. Pope, *Turbulent Flows* (Cambridge Univ. Pr., 2000).

[2]P. Sagaut and C. Cambon, *Homogeneous turbulence dynamics* (Springer, 2018).

[3]G. K. Batchelor and I. Proudman, "The effect of rapid distortion of a fluid in turbulent motion," Quart. J. Mech. Appl. Math. **7**, 83 (1954).

[4]M. J. Lee, "Distortion of homogeneous turbulence by axisymmetric strain and dilatation," Phys. Fluids **1**, 1541 (1989).

[5]L. Mahrt, "Stratified atmospheric boundary layers," Boundary-Layer Meteorol. **90**, 375 (1999).

[6]W. D. Smyth and K. B. Winters, "Turbulence and mixing in Holmboe waves," J. Phys. Oceanogr. **33**, 694 (2003).

[7]C. J. Hoogendoorn, "The effect of turbulence on heat transfer at a stagnation point," Int. J. Heat Mass Transfer **20**, 1333 (1977).

[8]L. J. Ayton and N. Peake, "Interaction of turbulence with the leading-edge stagnation point of a thin aerofoil," J. Fluid Mech. **798**, 436 (2016).

[9]S. Li, J. Li, Q. Yang, T. Li, P. Wang, and H. Huang, "Three-dimensional distortion of free-stream turbulence with the leading-edge stagnation point of an elongated bluff body," Phys. Fluids **36**, 125177 (2024).

[10]K.-S. Choi and J. L. Lumley, "The return to isotropy of homogeneous turbulence," J. Fluid Mech. **436**, 59 (2001).

[11]S. Liu, J. Katz, and C. Meneveau, "Evolution and modelling of subgrid scales during rapid straining of turbulence," J. Fluid Mech. **387**, 281 (1999).

[12]R. Hassanian, Á. Helgadóttir, L. Bouhlali, and M. Riedel, "An experiment generates a specified mean strained rate turbulent flow: Dynamics of particles," Phys. Fluids **35**, 015124 (2023).

[13]Z. Han, T. Watanabe, and K. Nagata, "Turbulence subject to axisymmetric expansion generated by opposed multiple-jet arrays," J. Fluid Mech. **1029**, A29 (2026).

[14]A. K. M. F. Hussain and V. Ramjee, "Effects of the axisymmetric contraction shape on incompressible turbulent flow," J. Fluids Eng. **98**, 58 (1976).

[15]T. Sjögren and A. V. Johansson, "Measurement and modelling of homogeneous axisymmetric turbulence," J. Fluid Mech. **374**, 59 (1998).

[16]S. Ayyalasomayajula and Z. Warhaft, "Nonlinear interactions in strained axisymmetric high-Reynolds-number turbulence," J. Fluid Mech. **566**, 273 (2006).

[17]Ö. Ertunç and F. Durst, "On the high contraction ratio anomaly of axisymmetric contraction of grid-generated turbulence," Phys. Fluids **20**, 025103 (2008).

[18]C. J. Zusi and J. B. Perot, "Simulation and modeling of turbulence subjected to a period of axisymmetric contraction or expansion," Phys. Fluids **26**, 115103 (2014).

[19]A. A. Alhareth, V. Mugundhan, K. R. Langley, and S. T. Thoroddsen, "Coherent turbulent structures in a rapid contraction," J. Fluid Mech. **1000**, A63 (2024).

[20]M. P. Clay and P. K. Yeung, "A numerical study of turbulence under temporally evolving axisymmetric contraction and subsequent relaxation," J. Fluid Mech. **805**, 460 (2016).

[21]J. Jiménez, A. A. Wray, P. G. Saffman, and R. S. Rogallo, "The structure of intense vorticity in isotropic turbulence," J. Fluid Mech. **255**, 65 (1993).

[22]R. Nagata, T. Watanabe, K. Nagata, and C. B. da Silva, "Triple decomposition of velocity gradient tensor in homogeneous isotropic turbulence," Comput. Fluids **198**, 104389 (2020).

[23]A. Vincent and M. Meneguzzi, "The dynamics of vorticity tubes in homogeneous turbulence," J. Fluid Mech. **258**, 245 (1994).

[24]J. Eisma, J. Westerweel, G. Ooms, and G. E. Elsinga, "Interfaces and internal layers in a turbulent boundary layer," Phys. Fluids **27**, 055103 (2015).

[25]T. Watanabe, K. Tanaka, and K. Nagata, "Characteristics of shearing motions in incompressible isotropic turbulence," Phys. Rev. Fluids **5**, 072601(R) (2020).

[26]P. A. Davidson, *Turbulence: An Introduction for Scientists and Engineers* (Oxford Univ. Pr., 2015).

[27]M. S. Chong, A. E. Perry, and B. J. Cantwell, "A general classification of three-dimensional flow fields," Phys. Fluids **2**, 765 (1990).

[28]J. Jeong and F. Hussain, "On the identification of a vortex," J. Fluid Mech. **285**, 69 (1995).

[29]J. Jiménez and A. A. Wray, "On the characteristics of vortex filaments in isotropic turbulence," J. Fluid Mech. **373**, 255 (1998).

[30]C. B. da Silva, R. J. N. Dos Reis, and J. C. F. Pereira, "The intense vorticity structures near the turbulent/non-turbulent interface in a jet," J. Fluid Mech. **685**, 165 (2011).

[31]M. Tanahashi, S. Iwase, and T. Miyauchi, "Appearance and alignment with strain rate of coherent fine scale eddies in turbulent mixing layer," J. Turbulence **2**, 1 (2001).

[32]R. Jahanbakhshi, N. S. Vaghefi, and C. K. Madnia, "Baroclinic vorticity generation near the turbulent/non-turbulent interface in a compressible shear layer," Phys. Fluids **27**, 105105 (2015).

[33]V. Kolář, "Vortex identification: New requirements and limitations," Int. J. Heat Fluid Flow **28**, 638 (2007).

[34]M. Hayashi, T. Watanabe, and K. Nagata, "Characteristics of small-scale shear layers in a temporally evolving turbulent planar jet," J. Fluid Mech. **920**, A38 (2021).

[35]D. Fiscaletti, O. R. H. Buxton, and A. Attili, "Internal layers in turbulent free-shear flows," Phys. Rev. Fluids **6**, 034612 (2021).

[36]R. Enoki, T. Watanabe, and K. Nagata, "Statistical properties of shear and nonshear velocity components in isotropic turbulence and turbulent jets," Phys. Rev. Fluids **8**, 104602 (2023).

[37]T. Passot, H. Politano, P. L. Sulem, J. R. Angilella, and M. Meneguzzi, "Instability of strained vortex layers and vortex tube formation in homogeneous turbulence," J. Fluid Mech. **282**, 313 (1995).

[38]T. Watanabe and K. Nagata, "Energetics and vortex structures near small-scale shear layers in turbulence," Phys. Fluids **34**, 095114 (2022).

[39]T. Watanabe and K. Nagata, "The response of small-scale shear layers to perturbations in turbulence," J. Fluid Mech. **963**, A31 (2023).

[40]T. Watanabe, "Efficient enhancement of turbulent entrainment by small-scale shear instability," J. Fluid Mech. **988**, A20 (2024).

[41]T. Watanabe and K. Nagata, "Influences of small-scale shear instability on passive-scalar mixing in a shear-free turbulent front," J. Fluid Mech. **1008**, A20 (2025).

[42]T. Watanabe, T. Mori, K. Ishizawa, and K. Nagata, "Scale dependence of local shearing motion in decaying turbulence generated by multiple-jet interaction," J. Fluid Mech. **997**, A14 (2024).

[43]C. J. Keylock, "The Schur decomposition of the velocity gradient tensor for turbulent flows," J. Fluid Mech. **848**, 876 (2018).

[44]P. Beaumard, O. R. H. Buxton, and C. J. Keylock, "The importance of non-normal contributions to velocity gradient tensor dynamics for spatially developing, inhomogeneous, turbulent flows," J. Turbul. **20**, 577 (2019).

[45]J. Kronborg and J. Hoffman, "The triple decomposition of the velocity gradient tensor as a standardized real Schur form," Phys. Fluids **35**, 031703 (2023).

[46]M. Takahashi, Y. Inagaki, K. Tsujimoto, and T. Ando, "Similar and dissimilar destruction of turbulent fluxes in a low-Reynolds-number channel flow," Phys. Fluids **37**, 015107 (2025).

[47]R. Arun and T. Colonius, "Velocity gradient partitioning in turbulent flows," J. Fluid Mech. **1000**, R5 (2024).

[48]R. Arun, M. Kamal, T. Colonius, and P. L. Johnson, "Normality-based analysis of multiscale velocity gradients and energy transfer in direct and large-eddy simulations of isotropic turbulence," J. Fluid Mech. **1021**, A47 (2025).

[49]D. C. Pack, "A note on Prandtl's formula for the wave-length of a supersonic gas jet," Q. J. Mech. Appl. Math. **3**, 173 (1950).

[50]T. Mori, T. Watanabe, and K. Nagata, "Nearly homogeneous and isotropic turbulence generated by the interaction of supersonic jets," Exp. Fluids **65**, 47 (2024).

[51]S. Ghahremanian, K. Svensson, M. J. Tummers, and B. Moshfegh, "Near-field mixing of jets issuing from an array of round nozzles," Int. J. Heat Fluid Flow **47**, 84 (2014).

[52]S. Tan, X. Xu, Y. Qi, and R. Ni, "Scalings and decay of homogeneous, nearly isotropic turbulence behind a jet array," Phys. Rev. Fluids **8**, 024603 (2023).

[53]T. Watanabe, T. Inagaki, T. Mori, K. Ishizawa, and K. Nagata, "Direct numerical simulations of the interaction of temporally evolving circular jets," J. Fluid Mech. **1009**, A68 (2025).

[54]N. T. Clemens and M. G. Mungal, "A planar Mie scattering technique for visualizing supersonic mixing flows," Exp. Fluids **11**, 175 (1991).

[55]A. Pizzaia and T. Rossmann, "Effect of boundary layer thickness on transverse sonic jet mixing in a supersonic turbulent crossflow," Phys. Fluids **30**, 115104 (2018).

[56]T. Kouchi, S. Fukuda, S. Miyai, Y. Nagata, and S. Yanase, "Acetone-condensation nanoparticle image velocimetry in a supersonic boundary layer," in *AIAA Scitech 2019 Forum* (2019) p. 1821.

[57]R. Theunissen, "Adaptive image interrogation for PIV: Application to compressible flows and interfaces," Ph.D. thesis, TU Delft, Delft University of Technology (2010).

[58]J. Westerweel and F. Scarano, "Universal outlier detection for PIV data," Exp. Fluids **39**, 1096 (2005).

[59]A. F. B. Inok, *Investigation of High-order, High-resolution Methods for Axisymmetric Turbulent Jet Using ILES*, Ph.D. thesis, Cranfield University, Cranfield, UK (2011).

[60]P.-Å. Krogstad and P. A. Davidson, "Is grid turbulence Saffman turbulence?" J. Fluid Mech. **642**, 373 (2010).

[61]J. C. Isaza, R. Salazar, and Z. Warhaft, "On grid-generated turbulence in the near-and far field regions," J. Fluid Mech. **753**, 402 (2014).

[62]T. Kitamura, K. Nagata, Y. Sakai, A. Sasoh, O. Terashima, H. Saito, and T. Harasaki, "On invariants in grid turbulence at moderate Reynolds numbers," J. Fluid Mech. **738**, 378 (2014).

[63]T. Watanabe and K. Nagata, "Integral invariants and decay of temporally developing grid turbulence," Phys. Fluids **30**, 105111 (2018).

[64]S. G. Saddoughi and S. V. Veeravalli, "Local isotropy in turbulent boundary layers at high Reynolds number," J. Fluid Mech. **268**, 333 (1994).

[65]K. Yamamoto, T. Ishida, T. Watanabe, and K. Nagata, "Experimental and numerical investigation of compressibility effects on velocity derivative flatness in turbulence," Phys. Fluids **34**, 055101 (2022).

[66]V. Mugundhan, R. S. Pugazenthi, N. B. Speirs, R. Samtaney, and S. T. Thoroddsen, "The alignment of vortical structures in turbulent flow through a contraction," J. Fluid Mech.

884, A5 (2020).

[67]A. A. Alhareth, V. Mugundhan, K. R. Langley, and S. T. Thoroddsen, "Turbulent structure and circulation inside different planar contractions," Phys. Fluids **36**, 075129 (2024).

[68]M. Hayashi, T. Watanabe, and K. Nagata, "The relation between shearing motions and the turbulent/non-turbulent interface in a turbulent planar jet," Phys. Fluids **33**, 055126 (2021).

[69]C. B. da Silva and J. C. F. Pereira, "Invariants of the velocity-gradient, rate-of-strain, and rate-of-rotation tensors across the turbulent/nonturbulent interface in jets," Phys. Fluids **20**, 055101 (2008).

[70]M. van Reeuwijk and M. Holzner, "The turbulence boundary of a temporal jet," J. Fluid Mech. **739**, 254 (2014).

[71]R. R. Taveira and C. B. da Silva, "Kinetic energy budgets near the turbulent/nonturbulent interface in jets," Phys. Fluids **25**, 015114 (2013).

[72]T. Watanabe, C. B. da Silva, Y. Sakai, K. Nagata, and T. Hayase, "Lagrangian properties of the entrainment across turbulent/non-turbulent interface layers," Phys. Fluids **28**, 031701 (2016).

[73]T. Watanabe, C. B. da Silva, K. Nagata, and Y. Sakai, "Geometrical aspects of turbulent/non-turbulent interfaces with and without mean shear," Phys. Fluids **29**, 085105 (2017).

[74]M. Gauding, F. Dietzsch, J. H. Goebbert, D. Thévenin, A. Abdelsamie, and C. Hasse, "Dissipation element analysis of a turbulent non-premixed jet flame," Phys. Fluids **29**, 085103 (2017).

[75]S. Er, J.-P. Laval, and J. C. Vassilicos, "Length scales and the turbulent/non-turbulent interface of a temporally developing turbulent jet," J. Fluid Mech. **970**, A33 (2023).

[76]Y. Xie, X. Zhang, X.-L. Xiong, and Y. Zhou, "Temporal evolution of the turbulence interface of a turbulent plane jet," J. Fluid Mech. **1001**, A39 (2024).

[77]S. A. Stanley, S. Sarkar, and J. P. Mellado, "A study of the flow-field evolution and mixing in a planar turbulent jet using direct numerical simulation," J. Fluid Mech. **450**, 377 (2002).

[78]O. Terashima, Y. Sakai, and K. Nagata, "Simultaneous measurement of all three velocity components and pressure in a plane jet," Meas. Sci. Technol. **25**, 055301 (2014).

[79]T. Watanabe, Y. Sakai, K. Nagata, and Y. Ito, "Large eddy simulation study of turbulent

kinetic energy and scalar variance budgets and turbulent/non-turbulent interface in planar jets," Fluid Dyn. Res. **48**, 021407 (2016).

[80] T. Watanabe, X. Zhang, and K. Nagata, "Turbulent/non-turbulent interfaces detected in DNS of incompressible turbulent boundary layers," Phys. Fluids **30**, 035102 (2018).

[81] M. Klein, A. Sadiki, and J. Janicka, "Investigation of the influence of the Reynolds number on a plane jet using direct numerical simulation," Int. J. Heat Fluid Flow **24**, 785 (2003).

[82] O. Terashima, Y. Sakai, and K. Nagata, "Simultaneous measurement of velocity and pressure in a plane jet," Exp. Fluids **53**, 1149 (2012).

[83] T. Watanabe, Y. Sakai, K. Nagata, and O. Terashima, "Experimental study on the reaction rate of a second-order chemical reaction in a planar liquid jet," AIChE J. **60**, 3969 (2014).

[84] T. Watanabe, Y. Sakai, K. Nagata, Y. Ito, and T. Hayase, "Vortex stretching and compression near the turbulent/nonturbulent interface in a planar jet," J. Fluid Mech. **758**, 754 (2014).

[85] T. Watanabe, H. Abreu, K. Nagata, and C. B. da Silva, "Small-scale shear layers in isotropic turbulence of viscoelastic fluids," J. Fluid Mech. **1005**, A14 (2025).